Electrical Interconnects Based on Delafossite Thin Films

2023 CNF REU Intern: Paul Bloom
Intern Affiliation: Optical Engineering, University of Rochester

CNF REU Principal Investigator: Dr. Hari Nair, Materials Science and Engineering, Cornell University

CNF REU Mentor: Bilal Azhar, Chemical and Biomolecular Engineering, Cornell University

Program & Primary Source of Research Funding: 2023 Cornell NanoScale Facility Research Experiences for Undergraduates (CNF REU) Program via the National Science Foundation under Grant No. NNCI-2025233

Contact: pbloom2@u.rochester.edu, hn277@cornell.edu, ba428@cornell.edu

Website(s): https://cnf.cornell.edu/education/reu/2023

Primary CNF Tools Used: Veeco Savannah ALD, Woollam RC2 Spectroscopic Ellipsometer, Rapid Thermal Anneal - AG Associates Model 610, Everbeing SR-4 4-Point Probe Station

Abstract:

The dramatic increase in the resistivity of three-dimensional (3D) metal interconnects with decreasing dimensions presents a significant bottleneck for further downscaling of integrated circuits [1]. This rise in resistivity is due to increased interface electron scattering as the interconnect dimensions approach their electron mean free path. Metallic delafossite oxides, specifically $PtCoO_2$ and $PdCoO_2$, present an alternative solution due to their Quasi-2D nature which mitigates interface electron scattering due to a 2D Fermi surface (Figure 1). Synthesis of high quality single-crystal delafossite thin films has been previously demonstrated by molecular beam epitaxy (MBE) [2], however, the challenge remains to demonstrate similarly high quality growth with a back-end-of-the-line (BEOL) synthesis technique such as atomic layer deposition (ALD).

We want to realize high quality single-crystal ALD synthesis of $PtCoO_2$ for which we need to develop a ternary ALD process made up of the PtO and Co_xO_y binary cycles, with overlapping processing conditions. In this study, we will present on the development of the Co_xO_y binary cycles under favorable conditions for ternary $PtCoO_2$ growth. We optimized Co_xO_y growth with respect to temperature, Co-pulse length, O_3 exposure time, purging conditions, adhesion layer, and the number of cycles. We characterized the growth with ellipsometry, X-ray diffraction, and X-ray reflectivity.

Summary of Research:

To grow high-quality, single-crystal $PtCoO_2$ films, we had to determine the optimal ALD conditions for the $PtCoO_2$ process, which combined Co_xO_y and PtO binary cycles. The Co_xO_y binary cycle was calibrated at a substrate temperature suitable for deposition of PtO to support our ternary deposition process. Temperature windows with the Cobalt precursor Bis(N,N''-di-i-propylacetamidinato)cobalt(II) [$Co(iPr\text{-}MeAMD)_2$] and O_3 as a co-reactant are documented above 200°C [3] while the Pt deposition process is characterized above 175°C at the Cornell NanoScale Science and Technology Facility (CNF) using the same deposition tool where we calibrated our Co_xO_y cycle.

We found growths per cycle (GPC) of Co_xO_y films at 150 and 175°C that were greater than growth values documented in literature at higher temperatures using similar processes (Figure 2). Increased GPC was observed by splitting up long precursor pulses into shorter, successive pulse/purge sub-cycles that resulted in the same cumulative precursor exposure (Figure 3). Linear GPC at substrate temperature of 150°C growth was observed without saturating O_3 vapor pressure, which indicated ALD growth, but yielded growth rates an order of magnitude lower than with a saturated O_3 pulse (Figure 4).

Deposition of Co_xO_y was calibrated on an Al_2O_3 adhesion layer as well as native SiO_2 layer and no difference in film growth was observed. The N_2 flow rate of the chamber was determined not to affect the film growth because the ratio of precursor to carrier gas remained constant and residence time of the precursor did not increase. With an unsaturated O_3 co-reactant vapor pressure, we found Co saturation at 0.5 seconds, but with very low GPC.

$PtCoO_2$ films were grown via ALD at an increased O_3 vapor pressure, but preliminary anneals in oxygen — measured using X-ray diffraction (XRD) — did not yield crystalline $PtCoO_2$ films.

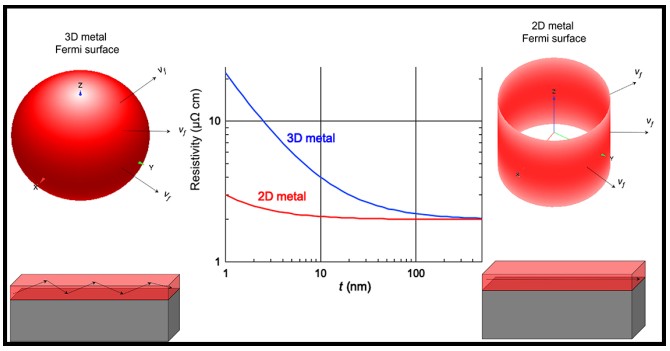

Figure 1: The quasi-2-dimensional crystal structure of the metallic delafossite oxides yield a nearly cylindrical Fermi surface with limited electron mobility out-of-plane. 3D metals (such as Cu) have a nearly spherical Fermi surface. We expect to see that the thickness of these interconnects will have a less dramatic impact on the resistivity of our quasi-2D material films.

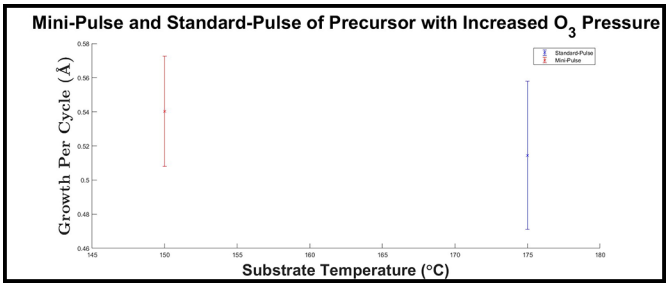

Figure 2: GPC plotted against substrate temperature at an increased O_3 pressure showing a growth rate greater than literature values documented at higher substrate temperatures.

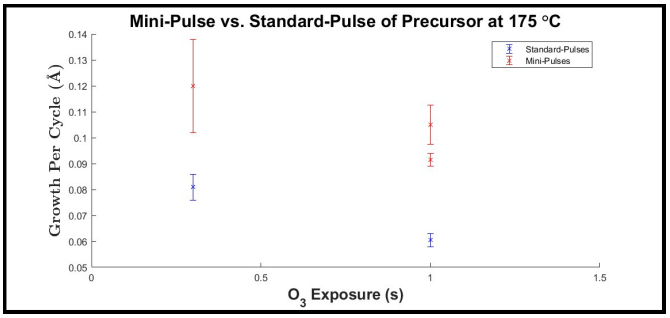

Figure 3: Increased GPC is shown using mini-precursor-pulses and multiple O_3 exposures.

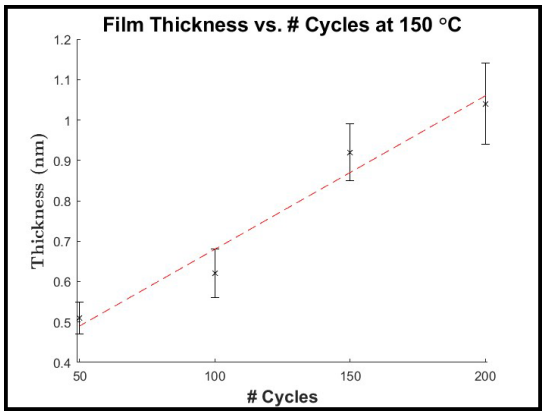

Figure 4: Average Co_xO_y film thickness vs. number of cycles at 150°C substrate temperature. Co_xO_y film thickness was measured at 65 points across a wafer using ellipsometry with a fixed refractive index. Co_xO_y thickness accounts for any adhesion layer (Al_2O_3) and native SiO_2.

Conclusions and Future Steps:

So far, we have shown Co_xO_y ALD growth at suitable temperature for ternary $PtCoO_2$ supercycle and determined that mini-precursor-pulses greatly increase GPC of binary ALD processes. We have also calibrated this cycle at 150°C, which we believe would overlap with the PtO binary cycle.

We must now calibrate the PtO binary cycle to determine the ratio between binary cycles in our supercycle that will yield optimal $PtCoO_2$ films. After we deposit amorphous $PtCoO_2$, we must anneal the films to achieve our desired crystallinity. We must calibrate the annealing conditions of these films to produce single-crystal $PtCoO_2$ films without PtO or Co_xO_y contamination. We will also measure the electrical properties of these films at varying thickness to assess the resistivity scaling curves of these materials at decreasing dimensions.

Acknowledgements:

Special thanks to the Cornell NanoScale Science & Technology Facility Research Experiences for Undergraduates (CNF REU) Program for hosting this internship and to the CNF staff for their support. Many thanks to the Nair Research Group for their mentorship. This work was funded in part by the National Science Foundation via grant no. NNCI-2025233.

References:

[1] D. Gall, J. Appl. Phys. 127, 050901 (2020).
[2] J. Sun, M.R. Barone, C.S. Chang, M.E. Holtz, H. Paik, J. Schubert, D.A. Muller, and D.G. Schlom, APL Mater. 7, 121112 (2019).
[3] Wan, Z., Zhang, T. F., Zeng, Z., Xi, B., Atomic Layer Deposition of CoxOy Films: Oxidants versus Composition. Adv. Mater. Interfaces 2022, 9, 2200097. https://doi.org/10.1002/admi.202200097.

Etching of Topological Metals for Interconnect

2023 CNF REU Intern: Astrid Dzotcha Kengne
Intern Affiliation: Electrical Engineering, Morgan State University

CNF REU Principal Investigator: Prof. Jeeyoung Judy Cha, Materials Science and Engineering, Cornell University

CNF REU Mentors: Gangtae Jin, Han Wang, Quynh P. Sam; Materials Science and Engineering, Cornell University

Program & Primary Source of Research Funding: 2023 Cornell NanoScale Science Facility Research Experiences for Undergraduates (CNF REU) Program via the National Science Foundation under Grant No. NNCI-2025233

Contact: asdzo1@morgan.edu, jc476@cornell.edu, gj98@cornell.edu, hw578@cornell.edu, qps2@cornell.edu

Website(s): https://cnf.cornell.edu/education/reu/2023

Primary CNF Tools Used: Scanning electron microscope (SEM), Nabity Nanometer Pattern Generator System, Reactive Ion Etcher PT720, Atomic Force Microscope (AFM), RC2 ellipsometer

Abstract:

On-chip interconnects are electrical wiring systems that connects transistors and other components in an integrated circuit. Copper (Cu) has been our main interconnect for over two decades. Over the years, the dimensions of Cu interconnects have decreased for better computing performance, and finally Cu has reached its limitations where under 15 nm of the interconnect width, signal delays and larger energy consumptions are significant due to the high resistivity of Cu interconnects stemming from surface and grain boundary scattering of electrons.

In contrast, topological metals, especially molybdenum phosphide (MoP), have shown promise as our next interconnect metals owing to their topological surface states that are resistant to scattering. We convert molybdenum sulfide (MoS_2) flakes to MoP by chemical vapor deposition and use electron beam and etching to create narrow nanoribbons. Four-point probe measurements show the resistivity to be 13 microohm-cm, demonstrating the viability of MoP as future interconnects.

Summary of Research:

Within the first two weeks of the program, we had several conferences, an in-person safety training course, a general online chemical safety training and lastly a cleanroom safety training while simultaneously reading relevant publications.

First, we got trained in the atomic force microscope (AFM). Then we got trained on the scanning electron microscope (SEM) with Nabity alongside. Later we were trained on how to use the RC2 ellipsometer. Then we were trained in the reactive ion etcher (RIE), specifically the PT720 Model.

And lastly, we were trained on the electron beam evaporator that uses a method of deposition to deposit various metals on wafers.

To start, our group already had silicon (Si) wafers coated with silicon dioxide (SiO_2) which only required us to clean the wafer to use. After cleaning the wafer using acetone and N-Methylpyrrolidone (NMP) for three minutes each, we exfoliated $MoSi_2$ on the SiO_2/Si wafer by pressing $MoSi_2$ crystals on the coated wafer using a double-sided tape.

We would then put our substrate under an optical microscope (OM) to see if any flake can potentially be used for the project. The flake would then be transferred to another wafer using either wet or dry transfer. This process was done by my mentors (Gangtae and Han) because it involved hydrofluoric acid (HF).

Later, using phosphine gas (Ph_3) in a tube furnace for one and a half hours, we were able to convert $MoSi_2$ to MoP. Shortly, after determining the thickness of our MoP flake under the AFM and optical microscope, we can now use a computer aided design (CAD) to cut out our desired width which was < 300 nm. Then protect our sample with 495 PMMA A4 resist by spin coating the wafer and baking it for two minutes at 2000 revolutions per minute (rpm) twice.

Then using the electron-beam and reactive ion etcher (RIE) etcher, we exposed and etched the target areas on the flake to get our desired width. We looked under both the AFM and the OM to see if both of those processes were successful. If we were successful, we then developed our samples in acetone for five to six hours to remove any residual resist. We then had to re-coat our sample with PMMA to prepare for the next e-beam exposure. This consisted of patterning 4-probe electrodes using CAD. Then go through the e-beam process to allow us to deposit

chromium (Cr) and gold (Au) using the e-beam evaporator to facilitate contact when measuring the nanowire's resistivity. If the second e-beam process was successful, we would then develop the sample with isopropyl alcohol (IPA) for about two minutes or less to see if the exposure was successful so we can do deposition then measure the resistivity of the nanowire.

Conclusions and Future Steps:

We successfully fabricated our narrow MoP nanoribbons to determine the resistivity of MoP under 20 nm. The resistivity of the etched nanoribbon was high, possibly due to damage during the fabrication process.

Potential improvements to this process include exploring other etching processes and limiting ambient exposure during the whole fabrication process. Also use X-ray diffraction (XRD) throughout the fabrication process to determine whether our sample changed states or if it remains MoP throughout the fabrication process.

Acknowledgements:

A.D.K. acknowledges the support from the National Science Foundation REU program. The project made use of the Cornell NanoScale Science and Technology Facility supported by the NSF grant no. NNCI-2025233. Characterization of the samples was carried out at Cornell Center for Materials Research. Many thanks to Judy J. Cha as the principal investigator.

References:

[1] Gall, D., Cha, J.J., Chen, Z. et al. Materials for interconnects. MRS Bulletin 46, 959-966 (202jj1). https://doi.org/10.1557/s43577-021-00192-3.

[2] Han, H. J., Kumar, S., Jin, G., Ji, X., Hart, J. L., Hynek, D. J., Sam, Q. P., Hasse, V., Felser, C., Cahill, D. G., Sundararaman, R., Cha, J. J., Topological Metal MoP Nanowire for Interconnect. Adv. Mater. 2023, 35, 2208965. https://doi.org/10.1002/adma.202208965.

[3] Wang, W., Qi, J., Zhai, L., Ma, C., Ke, C., Zhai, W., Wu, Z., Bao, K., Yao, Y., Li, S., Chen, B., Repaka, D. V. M., Zhang, X., Ye, R., Lai, Z., Luo, G., Chen, Y., He, Q., Preparation of 2D Molybdenum Phosphide via Surface-Confined Atomic Substitution. Adv. Mater. 2022, 34, 2203220. https://doi.org/10.1002/adma.202203220.

[4] Wang, W., Qi, J., Zhai, L., Ma, C., Ke, C., Zhai, W., Wu, Z., Bao, K., Yao, Y., Li, S., Chen, B., Repaka, D. V. M., Zhang, X., Ye, R., Lai, Z., Luo, G., Chen, Y., He, Q., Preparation of 2D Molybdenum Phosphide via Surface-Confined Atomic Su.

[5] Wang, J., Wu, Z., Mao, C. et al. Effect of Electrical Contact Resistance on Measurement of Thermal Conductivity and Wiedemann-Franz Law for Individual Metallic Nanowires. Sci Rep 8, 4862 (2018). https://doi.org/10.1038/s41598-018-23291-9.

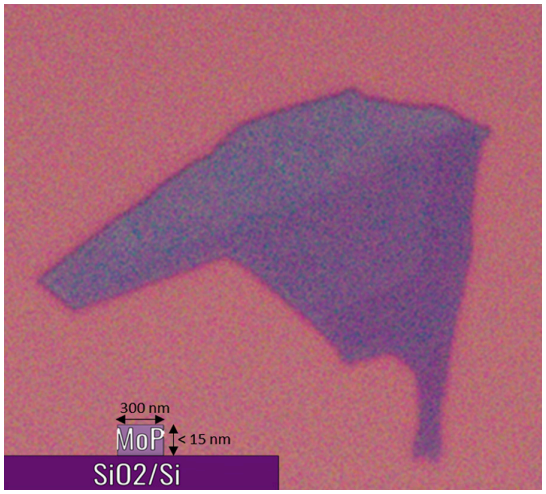

Figure 1: MoP flake.

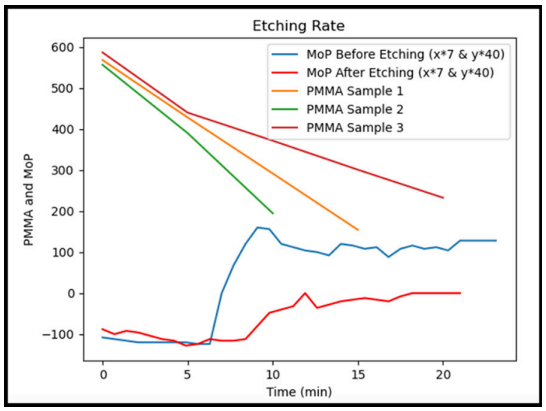

Figure 2: PMMA and MoP etching.

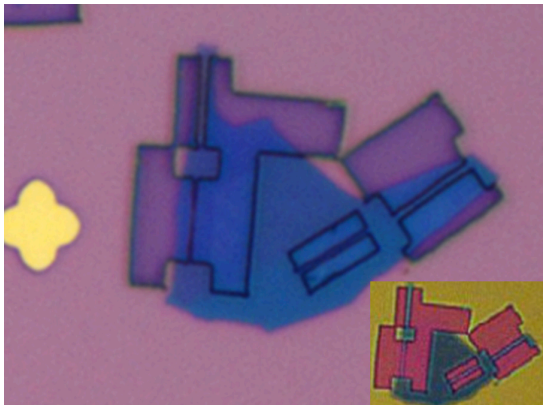

Figure 3: MoP before and after etching.

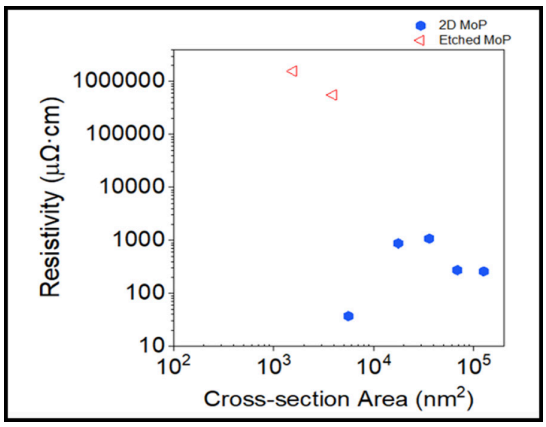

Figure 4: Resistivity measurement.

Palladium Thin Films for Hydrogen-Driven Actuation and Liquid Crystal Sensing in Microrobotics

2023 CNF REU Intern: Bryan Junsuh Kim
Intern Affiliation: Chemistry, University of California, Berkeley

CNF REU Principal Investigator: Nicholas Lawrence Abbott, Chemical & Biomolecular Engineering, Cornell
CNF REU Mentor(s): Hanyu Alice Zhang, Ayushi Tripathi; Physics, Chemical & Biomolecular Engineering, Cornell
Program & Primary Source of Research Funding: 2023 Cornell NanoScale Facility Research Experiences for Undergraduates (CNF REU) Program via the National Science Foundation under Grant No. NNCI-2025233
Contact: bryanjskim@berkeley.edu, nla34@cornell.edu, hz496@cornell.edu, at885@cornell.edu
Website(s): https://cnf.cornell.edu/education/reu/2023
Primary CNF Tools Used: AJA3 Sputtering Deposition, ABM Contact Alignment, Zeiss SEM, Bruker Energy Dispersive X-ray Spectroscopy (EDS), Oxford PECVD, Critical Point Dryer

Abstract:

Microrobots rely on actuation and sensing as two key functions to navigate their environment. Chemomechanical actuation leverages gaseous fuels such as hydrogen to drive mechanical movement, while liquid crystals can sense hydrogen by generating an optical signal. Here, we study sputter-deposited thin films of palladium for micron-scale actuation and liquid crystal responsive sensors. Through a photolithographic process, we fabricate a palladium-titanium bimorph hinge between two silicon dioxide (SiO_2) panels, one fixed while the other free to rotate, as a working microactuator device. By exposing the microhinge to gaseous hydrogen, hydrogen diffuses into the palladium bulk and induces a phase transition from a hydrogen-poor alpha (α) phase to a hydrogen-rich beta (β) phase in which the lattice parameter increases from 3.89 angstroms (Å) to 4.03 Å, bringing about a volumetric expansion that drives actuator bending. To promote faster actuation, we also introduce gold to create a palladium-gold alloy hinge, for the palladium-gold-hydride system facilitates a second-order phase transition with an alloy composition of 15-20% gold. Furthermore, our study reveals that sputter-deposited palladium induces surface anisotropy, observed via a preferential azimuthal direction of the liquid crystals when planarly aligned by hydrogen.

Summary of Research:

This research was conducted across two channels: fabricating microactuator devices and running hydrogen experiments for liquid crystal sensing.

Based on a past study in the Abbott group, the chemomechanical actuator device was composed of a platinum-titanium hinge between two SiO_2 panels: one fixed while the other free to rotate [1]. By applying gaseous hydrogen or oxygen, platinum surface stress drives reversible curvature changes for microactuation. A merit of chemomechanical actuation is the circumvention of intermediate conversion processes (unlike photovoltaic actuators that convert light to voltage, then voltage to mechanical bending).

Here, platinum was switched out for palladium. Because gaseous species only interact with the platinum surface, the bending curvature is relatively weak. On the other hand, hydrogen diffuses into the palladium bulk and facilitates a phase transition from hydrogen-poor α-phase to hydrogen-rich β-phase. An increase in unit cell lattice parameter from 3.89Å to 4.03Å results in increased bulk volume [2]. Through bulk volumetric expansion instead of surface stress, a palladium-based actuator hinge can drive stronger mechanical bending than a platinum-based actuator hinge.

Through a photolithographic process, the palladium hinge actuators were fabricated. Two square SiO_2 panels, ten microns (μm) in length, were attached to a palladium-titanium hinge with dimensions 10 μm by 5 μm in length. The hinge was made by sputtering 50 nanometers (nm) of palladium on 10 nm of titanium. Additionally, a tether was attached to the bottom SiO_2 panel for support.

After fabrication, the devices were exposed to cycles of hydrogen and air. As observed in Figure 1, the actuation was gradual over three minutes of hydrogen exposure. Furthermore, the curvature change is jolty and abrupt rather than linear and smooth.

To remediate, gold was incorporated into the palladium hinge. In the palladium-hydride system, the transition from α to β is characterized by a 1st-order phase transition. Because the two phases must nucleate separately, an energy barrier exists. In the palladium-gold-hydride system, however, a 2nd-order phase transition is facilitated, meaning that phase separation is lost and the energy barrier is minimized. This absence of phase separation can lead to smoother, faster actuation.

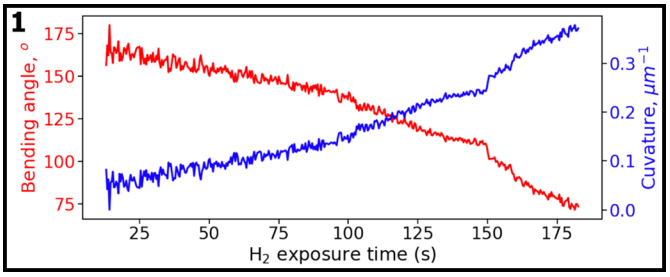

Figure 1: Hydrogen response for the Pd actuator hinge. Bending angle is defined as the angle between the two SiO_2 panels, and curvature is the change in the angle of deformation per unit length.

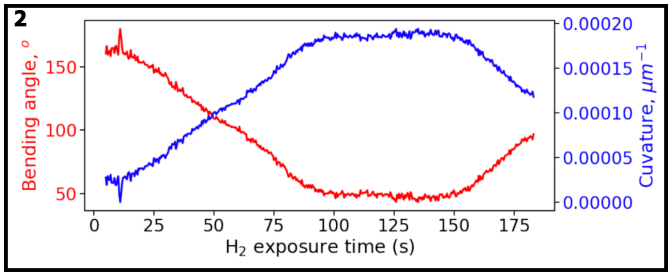

Figure 2: Hydrogen response for the palladium-gold actuator hinge.

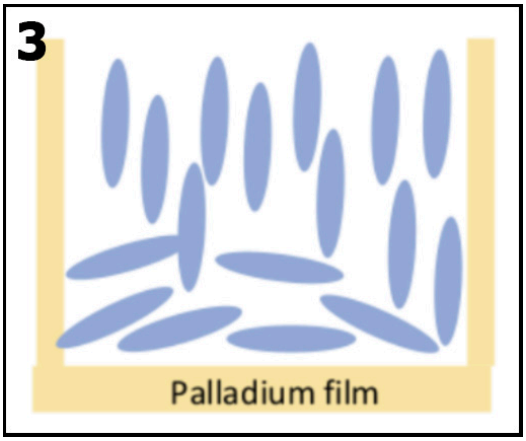

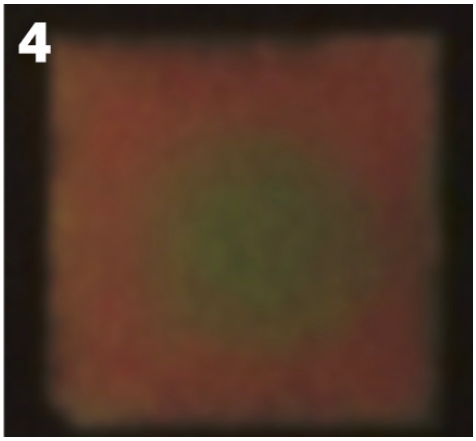

Figure 3, left: Side view of a schematic of planarly-aligned 5CB liquid crystals on the surface of sputtered palladium thin film. Figure 4, right: Top-down view of the bright optical response of 5CB liquid crystals on sputtered Pd.

From literature for the palladium-gold-hydride system, 15-20% gold concentration for a palladium-gold alloy is known to pass the critical point for phase separation [3].

The palladium-gold hinge was deposited via co-sputtering, which allowed tunable gold concentration. As shown in Figure 2, faster bending was observed over three minutes of hydrogen exposure. However, around 2.5 minutes, the hinge began to curve backwards, a behavior that remains to be investigated.

For liquid crystal sensing, 4-cyano-4'-pentylbiphenyl (5CB) liquid crystals were deposited on a sputtered palladium thin film. After two minutes of hydrogen exposure, the liquid crystals' surface alignment reoriented from homeotropic to planar as illustrated in Figure 3. The bright optical response is observed in Figure 4. Furthermore, it was discerned that the liquid crystals were uniformly aligned in a specific azimuthal direction. By rotating the sample along one of the cross-polarizer directions, the bright optical response briefly dimmed. Thus, sputtering deposition seems to induce surface anisotropy, observed by the preferential in-plane alignment of the liquid crystals.

Conclusions and Future Steps:

For the palladium-gold actuators, the hinge's behavior of curving backwards remains to be understood, necessitating fabrication of more palladium-gold actuator samples. A possible explanation is crack formation in the hinge, causing hydrogen to drive out and reverting the α-to-β volumetric expansion.

For liquid crystal sensing, the origins of the surface anisotropy induced by sputtering remain to be investigated. Sputtering instrumentation parameters, such as target-to-substrate distances and angles, could elucidate so, as well as understanding the surface grain shape, orientation, etc.

Acknowledgements:

I would like to acknowledge the National Science Foundation (NSF) grant no. NNCI-2025233, the National Nanotechnology Coordinated Infrastructure (NNCI), and the Cornell NanoScale Facility for funding and curating the Research Experiences for Undergraduates (CNF REU) opportunity. I would also like to acknowledge and thank Prof. Nicholas Abbott, Alice Zhang, Ayushi Tripathi, and Tom Pennell for their research mentorship, as well as Melanie-Claire Mallison for her guidance as REU coordinator.

References:

[1] Bao, N., et al. (2023). PNAS, 120(19).
[2] Wang, B., et al. (2021). Micromachines, 12(11).
[3] Maeland A., Flanagan, T.B. (1965). J. Phys. Chem., 1965, 69(10).

In-situ and *Ex-situ* Si Doping of β-Ga_2O_3

CNF Project Number: 150-82
Principal Investigator(s): Michael Thompson, Hari Nair
User(s): Cameron Gorsak, Katie Gann

Affiliation(s): Department of Materials Science and Engineering, Cornell University

Primary Source(s) of Research Funding: AFOSR/AFRL ACCESS Center of Excellence under Award No. FA9550-18-10529

Contact: cag284@cornell.edu, krg66@cornell.edu, mot1@cornell.edu, hn277@cornell.edu

Website(s): https://www.thompson.mse.cornell.edu/

Primary CNF Tools Used: DISCO Dicing Saw, Oxford ALD FlexAL

Abstract:

Recently, there is great interest in the material β-Ga_2O_3, which has an ultra-wide bandgap of ~ 4.8 eV. β-Ga_2O_3 is of interest for its application for radio frequency (RF), high power electronics, and solar-blind UV detectors. β-Ga_2O_3 substrates can be grown from the melt, which will make scaling-up production favorable. Additionally, the facile n-type doping of β-Ga_2O_3 is achieved due to the availability of shallow donors. In this work, we demonstrate controllable *in-situ* and *ex-situ* Si doping of β-Ga_2O_3, by MOCVD and ion-implantation respectively.

Summary of Research:

In this work, Fe doped β-Ga_2O_3 substrates were acquired from Novel Crystal Technology and then subsequently diced into a square geometry for Hall effect measurements, typically 5 × 5 or 10 × 10 mm.

In-situ Si doping was performed during the metal organic chemical vapor deposition (MOCVD) growth in an Agnitron Agilis 100 system. Figure 1 shows the controllability of *in-situ* Si doping by tuning the moles of Si per nm of β-Ga_2O_3 growth at a chamber pressure of 15 Torr. Doping is controlled over three orders of magnitude from mid × 10^{16} to low × 10^{19} cm^{-3} with competitive mobilities. Even higher *in-situ* doping up to 1 × 10^{20} cm^{-3} can be achieved by increasing the chamber pressure for 40 Torr to increase the cracking efficiency of the Si precursor, silane.

Ex-situ Si doping was performed by ion-implanted of unintentionally doped (UID) β-Ga_2O_3 grown by plasma-assisted molecular beam epitaxy (MBE). Prior to ion implantation, a 20 nm SiO_2 cap was deposited on the sample via atomic layer deposition (ALD) in order to tailor the Si implant profile. After ion implantation, the samples were annealed under a controlled ultra-high purity nitrogen ambient in order to activate the dopants. The best anneal condition was found to be 950°C for five minutes for implant concentrations between 5 × 10^{18} to 1 × 10^{20} cm^{-3}, achieving greater than 80% activation with mobilities all recovered to greater than 70 cm^2/ V • s for all conditions.

This work has laid the groundwork for current device processing by enabling high channel mobilities via *in-situ* doping and ohmic contacts via *ex-situ* ion implantation.

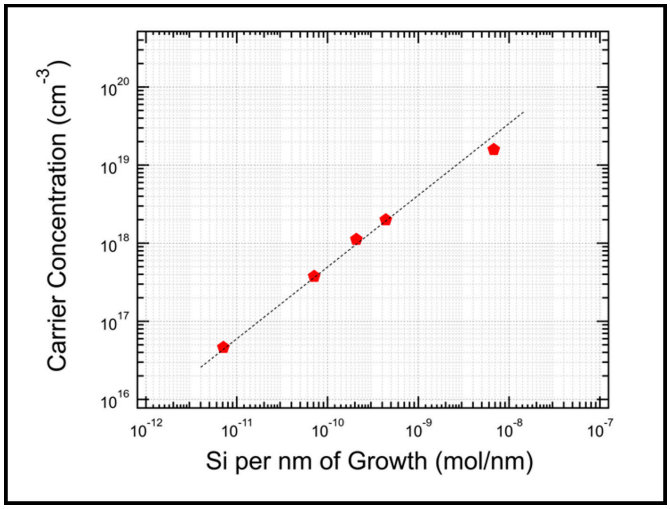

Figure 1: Demonstrated in-situ *Si doping concentration from mid × 10^{16} to low × 10^{19} cm^{-3} by controlling the molar flow of Si per nm of MOCVD* β-Ga_2O_3 *growth.*

The Effect of Nitrogen on the Stability of the β Phase in W Thin Films

CNF Project Number: 699-98
Principal Investigator(s): Shefford P. Baker
User(s): Yue Zhao, Jiayi Cao, Samantha Wang, Hannah Morgan-Smith Myers

Affiliation(s): Department of Materials Science and Engineering, Cornell University

Primary Source(s) of Research Funding: National Science Foundation DMR-1810138

Contact: shefford.baker@cornell.edu, yz2722@cornell.edu, jc2732@cornell.edu, mw842@cornell.edu, hem66@cornell.edu

Primary CNF Tools Used: AJA Sputter Deposition, FleXus Film Stress Measurement, P7 Profilometer, Dektak XT Profilometer, CDE ResMap Resistivity 4-pt Probe, Panalytical X-ray Diffractometer, Veeco Icon Atomic Force Microscope, Zeiss Supra Scanning Electron

Abstract:

The body centered cubic (BCC) phase (α-W) is the only known stable structure in tungsten. However, a metastable phase (β-W) having A15 structure can be produced using atom-by-atom deposition methods. Interest in the metastable phase recently spiked it has been shown to exhibit a giant spin Hall effect (GSHE) [1], which is expected to enable significant miniaturization in next-generation magnetoresistive random access memory (MRAM). To be useful in technology, it must be possible to reliably produce β-W and to retain it during production and use. It is known that inclusion of small amounts of nitrogen facilitates production of the β-phase [2] {Liu, 2016 #3025}. However, little is known about the stability of this metastable phase or how and why it forms. In this work we explore the effects of N on the formation and thermal stability of β-W. We deposit W films with different N contents in CNF and use x-ray diffraction to determine the fractions of α- and β-W before and after thermal cycling. Results are modeled to examine the kinetics and mechanisms of the β-α phase transformation.

Summary of Research:

Tungsten thin films were deposited onto 4" Si <100> wafers with native oxide using the AJA DC magnetron sputtering system in CNF and a 99.95% 3" W target. The Si wafers were plasma cleaned for 60 seconds before deposition. The base pressure was better than 2×10^{-8} Torr. Each film was sputtered at a power of 400 W in a working gas pressure of 3 mTorr for 1000 s. A total flow rate of 30 sccm of Ar and N was maintained with N flow rates of 0, 0.5, 1, 1.5, and 2 sccm. A temperature indicator was affixed to the back of the Si wafer to determine the maximum temperature the wafer reached during deposition. A "witness sample" of Si with a photoresist pattern was also attached to the substrate carrier. After deposition, the photoresist was lifted-off using acetone, and the thicknesses of the remaining W was measured using the Dektak® XT profilometer at CNF. The stresses in the as-deposited films were determined using the FleXus® film stress measurement instrument at CNF.

The as-deposited films were cleaved into 1 cm × 1 cm samples. Individual pieces were then heated at 10°C/min in a high vacuum furnace to temperatures of 300, 400, 500, 600 and 700°C, under a base pressure better than 10^{-7} Torr. No thermal oxidation was detected after the annealing.

The textures and phase fractions of α- and β-W were determined using x-ray diffraction on the as-deposited and the annealed samples. Symmetric 2θ scans were performed from 20° to 90° with a step size of 0.02°. Rocking curve scans using the ω geometry were obtained for all α and β peaks visible on the 2θ scans.

The deposited films had thicknesses of 190 ± 5 nm, the maximum temperature during the depositions was 66-71°C, and the stress in the as-deposited films was -2.3 to -2.1 GPa. Nitrogen concentrations in the as-deposited films were estimated from the flow rates to be 2.53, 4.95, 7.27, and 9.49 at% for films deposited in 0.5, 1.0, 1.5, and 2.0 sccm N_2, respectively.

For the as-deposited samples, all the 2θ diffraction peaks were identified as β, except for a small α(211) peak at 2θ = 73.193°. After thermal annealing, α(110) peaks emerged, indicating the initiation of the β to α transformation. With increasing annealing temperature, the intensities of the α peaks increase while those of the β peaks decrease. Eventually, all the β peaks vanished, indicating complete transformation to the α phase.

The rocking curves were analyzed to estimate the phase fractions in the samples. The phase fractions as a function of annealing temperature are shown in Figure 1. A Johnson-Mehl-Avrami-Kolmagorov type model

(similar to [3]) was developed to describe the phase transformation as a function of temperature in terms of the different activation energies involved. The results of the model are also shown in Figure 1.

Conclusions and Future Steps:

The model suggests that nitrogen stabilizes the β phase by accumulating in phase boundaries, slowing their motion. In the future, we will use CNF equipment to attempt to make N-free β-W films and to measure their properties (e.g., resistivity) as a function of N content.

References:

[1] Pai, C.F., L.Q. Liu, Y. Li, H.W. Tseng, D.C. Ralph, and R.A. Buhrman, Spin transfer torque devices utilizing the giant spin Hall effect of tungsten. Applied Physics Letters, 101(12) (2012).

[2] Liu, J. and K. Barmak, Topologically close-packed phases: Deposition and formation mechanism of metastable β-W in thin films. Acta Mater 104, 223-227 (2016).

[3] Denis, S., D. Farias, and A. Simon, Mathematical-Model Coupling Phase-Transformations and Temperature Evolutions in Steels. ISIJ International, 32(3) 316-325 (1992).

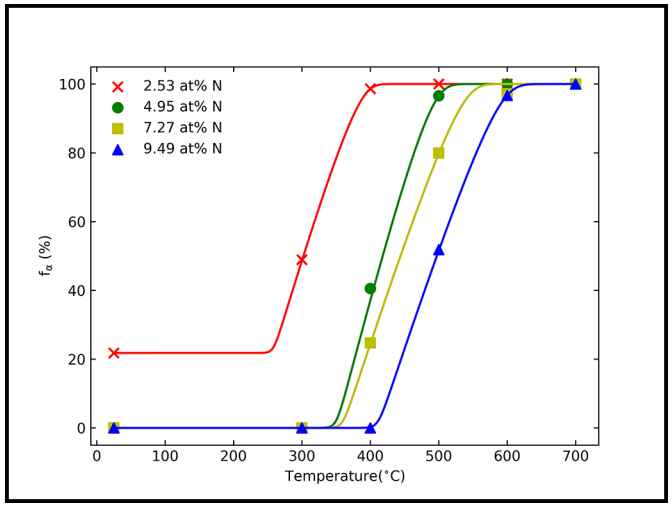

Figure 1: Volume fraction of α-W as a function of annealing temperature for films of varying N content. Points indicate experimental measurements, lines indicate results of a model.

Reactive Ion Etching (RIE) Reveals Biphasic Self-Assembled Mesostructures in Block Copolymer Thin Films

CNF Project Number: 1356-05
Principal Investigator(s): Ulrich Wiesner
User(s): Fei Yu

Affiliation(s): Department of Materials Science and Engineering, Cornell University

Primary Source(s) of Research Funding: U.S. Department of Energy (DOE), Office of Science (Basic Energy Sciences (DE-SC0010560)

Contact: ubw1@cornell.edu, fy84@cornell.edu

Website(s): http://wiesner.mse.cornell.edu/

Primary CNF Tools Used: Oxford 81 Etcher

Abstract:

The surface morphology of thin films of a triblock terpolymer was first characterized by atomic force microscopy, which shows a different mesostructure from the one suggested by small-angle X-ray scattering. Reactive ion etching by CF_4 plasma of the polymer film was carried out at CNF to bring out the substructure beneath the surface, which turned out to be biphasic. The plasma etching, combined with microcopy and scattering techniques, offers a powerful tool for a comprehensive probe of the self-assembled mesostructure inside the block copolymer thin films.

Summary of Research:

The surface morphology of block copolymer thin films can be characterized by scanning electron microscopy (SEM) or atomic force microscopy (AFM). It is challenging, however, to gain a real-space picture of the underlying structures with microscopy techniques. In our experiment, thin films of the triblock terpolymer poly(isoprene)-*block*-poly-(styrene)-*block*-poly(N,N-dimethylaminoethyl methacrylate) (PI-*b*-PS-*b*-PDMAEMA, or ISA) were prepared by spin-coating a 5.0 wt% solution in tetrahydrofuran (THF) onto a silicon wafer. After solvent vapor annealing (SVA) in THF for 19 h, Figure 1a,b shows the top surface morphology, as imaged with AFM. Films displayed periodically ordered hexagonal patterns with distinct regions attributed to each of the three blocks: PI?PS core?shell cylinders in a majority PDMAEMA matrix. Figure 2c,d depicts this structure schematically, with PI cylinder cores represented in green, PS cylinder shells in blue, and the PDMAEMA matrix in light pink.

In addition to the surface morphological characterization by AFM, grazing-incidence small-angle X-ray scattering (GISAXS) was performed to better understand the subsurface structures. The observed scattering pattern (Figure 2) was consistent with a core?shell double gyroid structure with the (211) planes parallel to the substrate and compressed 52% along [211] axis, i.e., along the film normal. The associated lattice parameters were as follows: a = 90.7 nm and $b = c$ = 121.4 nm, with angles α = 98° and $\beta = \gamma$ = 113°. According to the lattice parameters, the distance between neighboring (211) planes is 25.5 nm. Compression of the film was likely a result of rapid drying that occurred immediately upon the removal of samples from the SVA environment.

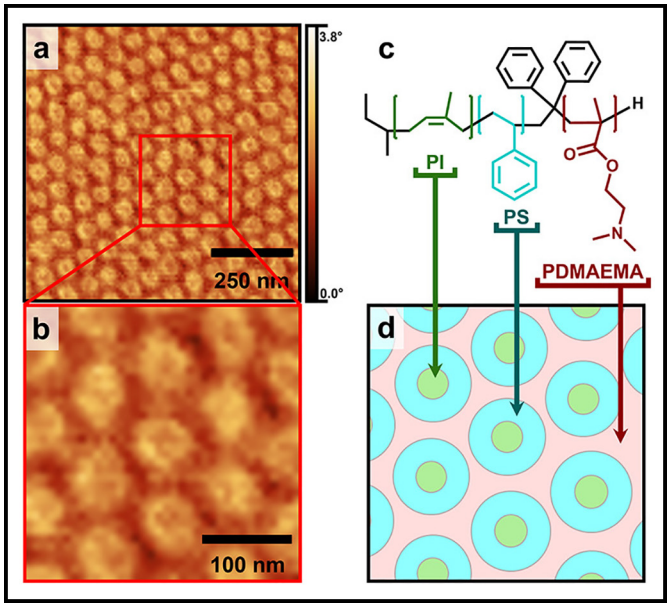

Figure 1: (a) AFM phase image of an ISA thin film. A magnified region marked with a red square in (a) is shown in (b), enabling identification of all three top surface blocks of the ISA structure depicted in (c). A schematic of the top surface morphology consistent with the AFM images is depicted in (d), showing PI cylinder cores (green), PS cylinder shells (blue), and the PDMAEMA matrix (light pink).

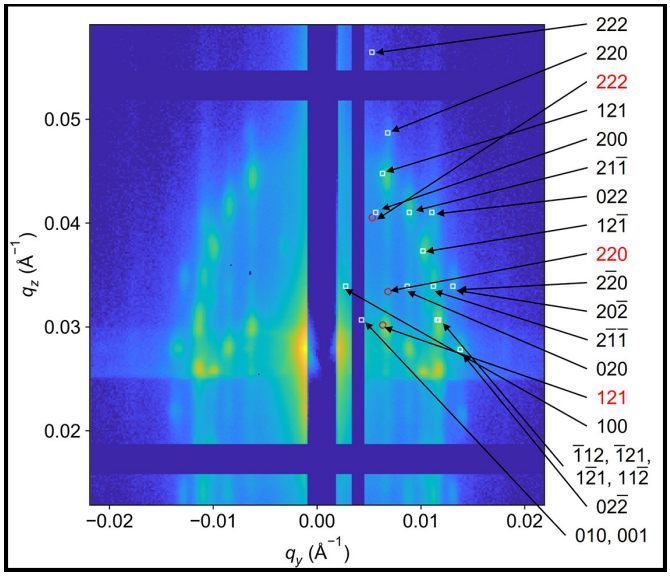

Figure 2: GISAXS patterns of an ISA thin film showing indexed peaks matching a double gyroid structure with the (211) plane parallel to the surface and compressed along the film normal. White squares and red circles correspond to expected peak positions through the reflection and transmission channels, respectively, in GISAXS.

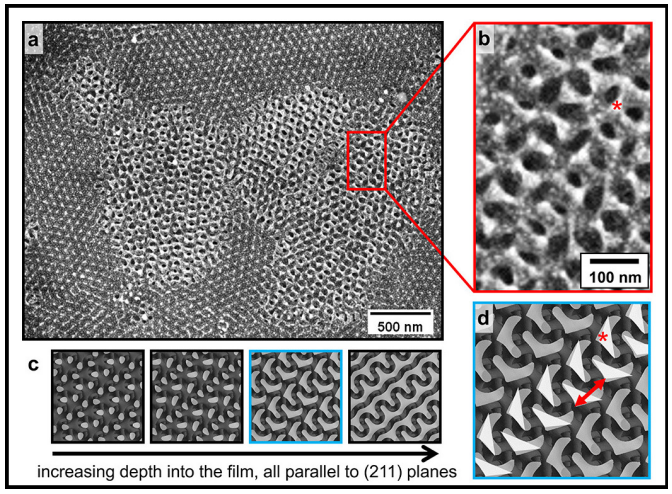

Figure 3: (a) SEM image with a selected area at higher magnification in the (b) red box of an ISA thin film surface after etching with CF_4 plasma for 7 s and (c) simulated (211) plane morphologies of the co-continuous double gyroid along the [211] axis at different depths. Comparing (d) a specific slice, outlined in blue, from the simulation stack to the area enlarged in (c) reveals clear similarities. Red asterisks in (b) and (d) indicate PI-rich locations that appear brighter in SEM due to preferential staining of the PI block with RuO_4. The red double arrow in (d) indicates the spacing between neighboring repetitive features in the (211) plane.

The GISAXS results suggest a different morphology from that revealed by AFM on the surface, but a straightforward comparison is difficult due to the scattering pattern in the reciprocal space. To reconcile these structural differences, it was of interest to investigate the change in structure when moving away from the top surface layer, i.e., deeper into the film. To visualize this transition, the thin films were etched with CF4 plasma and stained with RuO_4 for ~ 15 min to increase contrast in the subsequent SEM images. Figure 3a shows an SEM image of a film etched for 7 s. While there are still regions displaying hexagonal order, the image of the etched film now also clearly reveals areas that resemble a co-continuous structure. Regions with hexagonal lattice structure had a center-to-center cylinder distance of 71.2 ± 1.6 nm. The spacing between the neighboring repetitive features in the (211) plane (see red double arrow in Figure 3d) was 117.0 ± 4.1 nm, similar to the 112.7 nm spacing calculated from GISAXS data. Figure 3b shows an enlarged SEM image area that displays features consistent with a co-continuous structure. By comparing this pattern to simulated (211) planes of the double gyroid along the [211] axis at different depths (Figure 3c), a bent-triangular structure alternating from one side to another is clearly recognizable (see the blue box in Figure 3c). With the PI block stained more heavily as compared to PS, the corner marked with a red asterisk indicates a PI-rich location. These areas appear brighter in the SEM image from greater electron scattering and can be assigned to a similar structure in the simulation (compare Figure 3b,d). Therefore, reactive ion etching enables real-space microscopy characterization of underlying structures in self-assembled block copolymer thin films, which could differ from the surface.

References:

[1] Lee, W. Y., Chapman, D. V., Yu, F., Tait, W. R., Thedford, R. P., Freychet, G., Zhernenkov, M., Estroff, L. A., and Wiesner, U. B. (2022), Triblock Terpolymer Thin Film Nanocomposites Enabling Two-Color Optical Super-Resolution Microscopy. Macromolecules, 55(21), 9452-9464.

Low Loss Superconducting LC Resonator for Strong Coupling with Magnons

CNF Project Number: 2126-12
Principal Investigator(s): Gregory David Fuchs
User(s): Srishti Pal, Qin Xu, Varshith Kandula

Affiliation(s): Department of Applied Physics & Engineering, Department of Physics; Cornell University

Primary Source(s) of Research Funding: Department of Energy (DOE), Center for Molecular Quantum Transduction (CMQT)

Contact: gdf9@cornell.edu, sp2253@cornell.edu, qx85@cornell.edu, vk332@cornell.edu

Primary CNF Tools Used: AJA Sputter Deposition, Heidelberg Mask Writer - DWL2000, GCA 6300 DSW 5X g-line Wafer Stepper, YES Asher, AJA Ion Mill, PT770 Etcher - Left Side, P7 Profilometer, Zeiss Supra SEM, Nabity Nanometer Pattern Generator System (NPGS), JEOL 6300, Dicing Saw - DISCO, Westbond 7400A Ultrasonic Wire Bonder

Abstract:

We present a hybrid quantum system based on strong coupling between microwave photons host by micro-structured resonators and magnon modes of the molecular ferrimagnet vanadium tetracyanoethylene ($V[TCNE]_x$). Using Cornell NanoScale Facility (CNF), we develop a process to integrate the fabrication of thin-film superconducting LC resonators and the deposition of lithographically patterned $V[TCNE]_x$ films. We explore ways to enhance the quality factors of our LC resonators with the aim to elevate its performance in the strong coupling regime. We also focus on designing and fabricating new resonator structures capable of decoupled excitation and read-out of the hybrid magnonic system.

Summary of Research:

This research is focused on studying a strongly coupled hybrid photon-magnon system where the coupling strength between the two sub-systems exceeds the mean energy loss in either of them. The key figure-of-merit of this hybrid system is its cooperativity $C = 4g^2/\kappa_m\kappa_r$, where g is the coupling strength between magnons and photons, and κ_m and κ_r are the damping rates for magnons and photons, respectively. The system operates in strong-coupling regime if $C>1$.

In this work, we use lumped-element planar LC resonators fabricated on superconducting niobium thin-film offering high quality factor (Q-factor) and thus low κ_r. The basic steps for patterning our LC resonators using photolithography are shown in Figure 1(a). First, we sputter a 50 nm thick niobium film (thickness measured using P7 profilometer) on MOS cleaned sapphire substrate using AJA sputter. The superconducting transition temperature (T_c) of our niobium film comes out to be ~ 8.8K, which is high enough to offer low damping. The resonator design, patterned on a photomask using Heidelberg Mask Writer-DWL2000, is then cast onto the resist coated wafer (we spin-coat a resist bi-layer of LOR3A and S1813) using 5X g-line Stepper. The developed resist (in AZ726MIF) is descummed in the YES Asher followed by dry etching of niobium in AJA Ion Mill (and recently in PT770). Finally, we strip the resist in 1165 and dice the wafer using Dicing Saw-DISCO to separate the chips patterned on the wafer.

For the magnon sub-system, we use the low-loss organic ferrimagnet $V[TCNE]_x$ with a low Gilbert damping $\alpha \sim 10^{-4}$ offering long magnon lifetime and thus low κ_m. Using e-beam lithography in the JEOL 6300 or Nabity Nanometer Pattern Generator System (NPGS) connected to Zeiss Supra SEM, we pattern a 6 μm wide and 600 μm long bar on the 10 μm wide and 600 μm long inductor wire using the steps shown in Figure 1(b). We then ship the exposed resonator chips to our collaborators in Ohio State University for $V[TCNE]_x$ growth and liftoff.

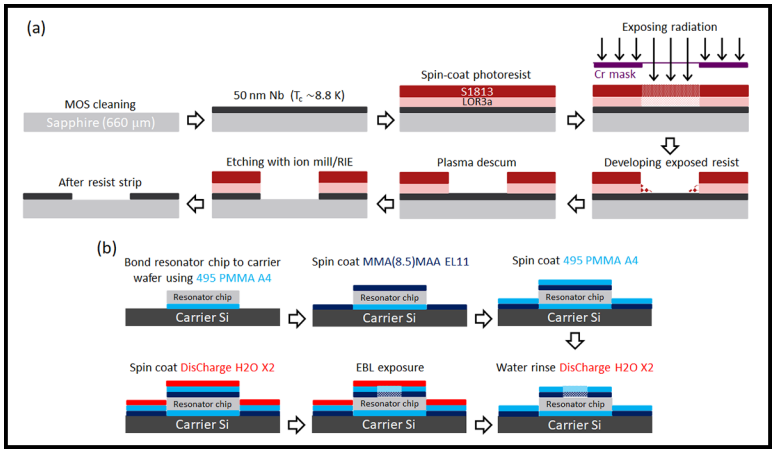

Figure 1: Process flow for (a) patterning the LC resonator using photolithography, and (b) e-beam patterning for $V[TCNE]_x$ deposition.

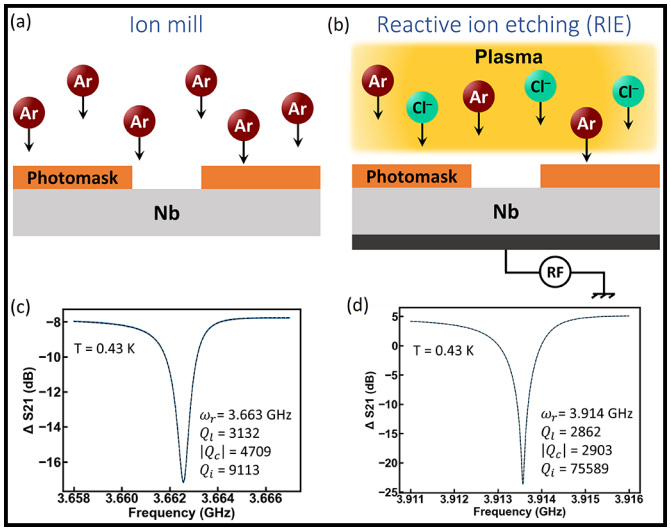

Figure 2: (a)-(b) The schematics of the ion mill and reactive ion etching processes, respectively. (c)-(d) Fitted resonator response with extracted Q-factors for the ion milled and reactive ion etched chips, respectively.

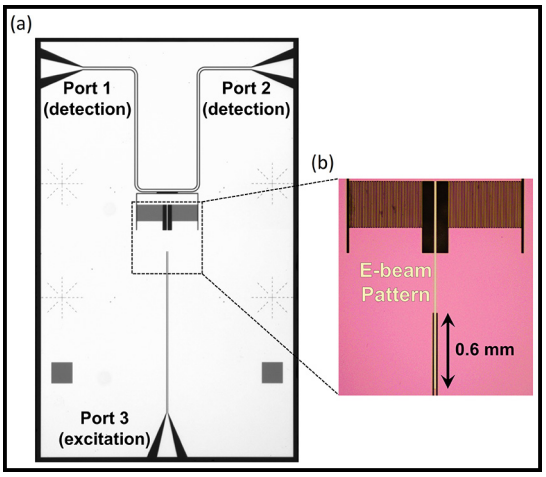

Figure 3: (a) Microscope image of the 3-port LC resonator with separated excitation and detection ports. (b) E-beam pattern with resist on (exposed and developed) for V[TCNE]$_x$ deposition.

The results on our first-generation coupled resonator-V[TCNE]$_x$ system are summarized in our recent arXiv article [1]. Our first-generation 2-port LC resonators were etched by ion milling (AJA Ion Mill) by neutral argon beam [Figure 2(a)]. The process of ion milling for our resonator design suffers from the drawbacks of — (i) slow overall etch-rate, (ii) non-uniform etch-rates at different parts of the design (especially drastically lower etch-rates for interdigitated capacitor fringes than that at other parts), (iii) substrate heating during the physical bombardment process of the high-energy Ar-beam, and (iv) possibly the etching residues of ejected niobium. These factors contributed to limit the internal Q-factor of our LC resonators to $\sim 10^3$ as shown in the transmission spectrum of Figure 2(c). The details of the fitting parameters are elucidated in reference [1]. To overcome the limitations of ion milling, we have recently adopted a chlorine-based reactive ion etching (RIE) process (PT770) shown in Figure 2(b). The key advantages of this etching method are — (i) extremely high etch-rates, (ii) uniform etching at all parts of the resonator, (iii) minimal heating of the substrate, and (iv) niobium is etched in the form of volatile niobium chlorides minimizing the contamination by residues. Upgradation to this RIE process resulted in an increase in the internal Q-factor of our LC resonators by a factor of ~ 8 [Figure 2(d)].

The performance of our old 2-port resonator design is limited due to the inseparable excitation and detection mechanism of the hybrid system. To get around this limitation, we have modified our resonator design where the V[TCNE]$_x$ bar is extended over a third port employed to excite the magnons without driving the resonator. The magnons are then expected to travel to the resonator which, in this case, can be used solely for sensing. Figure 3(a) shows our very first design for the 3-port resonators. We are currently in the process of optimizing this design with a primary goal of achieving high internal-Q, moderate co-operativity for the coupled magnon-resonator system, and a minimal crosstalk between the excitation port and the LC resonator system. The e-beam pattern for a future V[TCNE]$_x$ deposition on the 3-port resonator chip is shown in Figure 3(b).

Conclusions and Future Steps:

We have demonstrated the fabrication and integration of a low-loss hybrid photon-magnon system based on strong coupling between superconducting LC resonators and the organic ferrimagnet V[TCNE]$_x$. We have been able to enhance the intrinsic quality factor of our LC resonator by improved fabrication. We have further modified our resonator design for future experiments envisioned to disentangle the excitation and read-out mechanisms. After a successful optimization of our primordial 3-port resonator design, we plan to impose further modification to the design for developing experiments for magnon lasing and sensing magnon Bose-Einstein condensate (mBEC) states.

References:

[1] Q. Xu, H. F. H. Cheung, D. S. Cormode, T. O. Puel, H. Yusuf, M. Chilcote, M. E. Flatté, E. Johnston-Halperin, and G. D. Fuchs, "Strong photon-magnon coupling using a lithographically defined organic ferrimagnet", arXiv:2212.0442.

Ordering of Liquid Crystals on Photocatalytic Titania Surfaces

CNF Project Number: 2736-18
Principal Investigator(s): Prof. Nicholas L. Abbott
User(s): Ayushi Tripathi

Affiliation(s): Robert Frederick Smith School of Chemical and Biomolecular Engineering, Cornell University
Primary Source(s) of Research Funding: IIS-1837821, DMR-1921722
Contact: nla34@cornell.edu, at885@cornell.edu
Website(s): https://nlabbottcornell.weebly.com/
Primary CNF Tools Used: Arradiance ALD, Odd hour evaporator, Woollam RC2 Spectroscopic Ellipsometer

Abstract:

We have fabricated thin films of titania by atomic layer deposition (ALD). We used the photocatalytic activity of the films to design liquid crystalline systems that can be triggered to undergo orientational transitions upon illumination. Polarization modulation-infrared reflection-adsorption spectroscopy (PMIRRAS) was used to provide evidence that the orientational transitions arise from photocatalytic generation of a carboxylic acid-containing species in the liquid crystal. This study reports the first design of liquid crystalline systems that respond to the photocatalytic activity of metal oxide films.

Summary of Research:

We used the ALD process to fabricate titania (TiO_2) thin films using tetrakis(dimethylamino)titanium (TDMATi) and water (H_2O) as precursors and a deposition temperature of 225°C. After 60 cycles of deposition, we measured the ellipsometric thickness of the TiO_2 films to be 3.27±0.03 nm (Woollam spectroscopic ellipsometer). TiO_2 thin films were then annealed at 500°C for 15 h in air to obtain the anatase (101) phase of titania, as confirmed by X-ray diffraction analysis [1]. The films were also analyzed by X-ray photoelectron spectroscopy and the ratio of O to Ti was determined to be 2.04:1, consistent with the expected stoichiometry of titania [1].

The aim of our study was to couple photocatalytic reactions on the surface of titania with orientational transitions in liquid crystalline materials. Titania is a well-known photocatalyst with a wide band gap of 3.2 eV and is photoactive under UV illumination (<385 nm). We characterized the orientations of the nematic LC 4-cyano-4'-pentylbiphenyl (5CB) (structure shown in Figure 1(a)) on TiO_2(101) by preparing micrometer-thin films of 5CB on TiO_2(101) and characterizing their optical appearance using polarized light microscopy. We discovered that the orientations of 5CB on TiO_2(101) are dependent on ambient relative humidity (RH) levels. At low humidity (0-20% RH) or under dry conditions, 5CB exhibits a homeotropic (perpendicular) orientation on TiO_2(101) (Figure 1(b), (d)) whereas upon increasing RH, 5CB tilts away from the surface normal to ultimately assume a planar (parallel) orientation

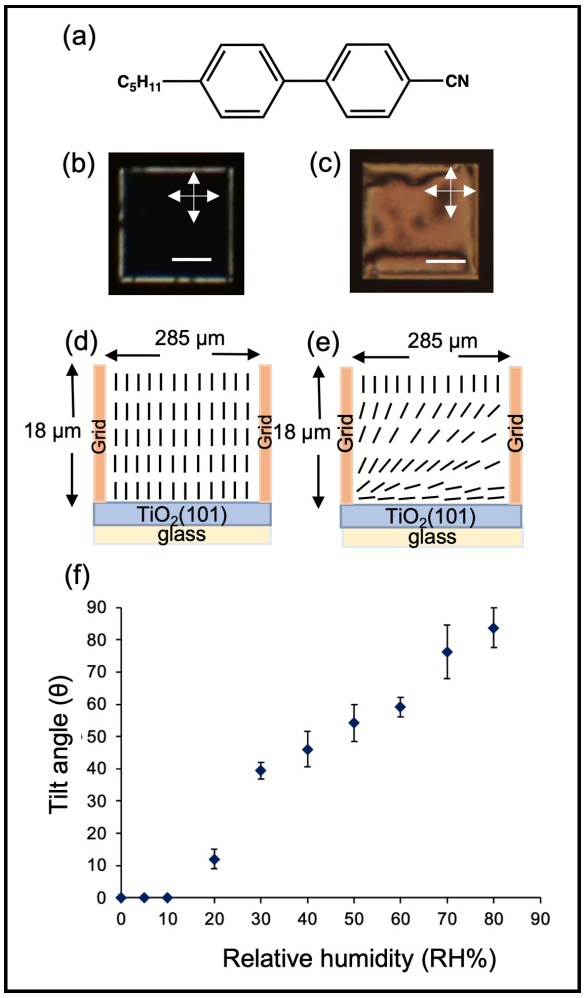

Figure 1: (a) Molecular structure of 4-cyano-4'-pentylbiphenyl (5CB). Optical micrographs (crossed polarizers) of 5CB hosted in copper grids on 3.27 ± 0.03 nm-thick films of TiO_2(101) under dry nitrogen conditions (b) and under 80% RH air (c). Schematic illustrations of director profiles of (d) homeotropic and (e) planar orientations of 5CB at TiO_2(101). (f) Plot of change in tilt angle of 5CB from surface normal on TiO_2(101) as a function of RH level. Scale bar: 100 µm.

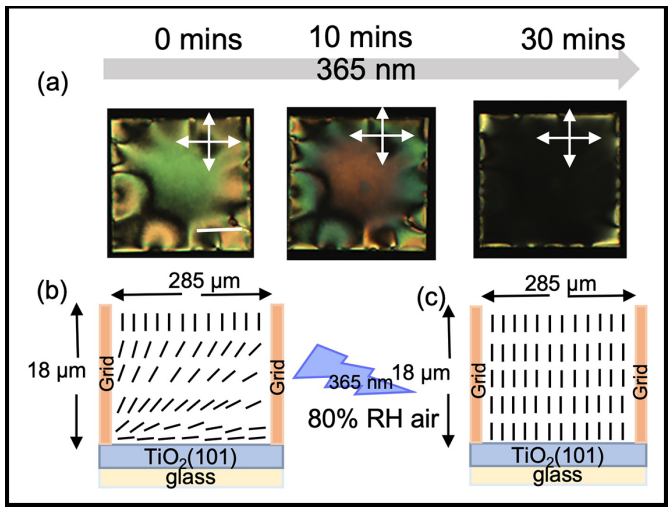

Figure 2: (a) Optical micrographs (crossed polarizers) of 5CB hosted in copper grids on 3.27 ± 0.03 nm-thick films of TiO_2(101) under 80% RH air upon illumination by a UV lamp of wavelength 365 nm and intensity 1.8 mW/cm² at time 0 mins, 10 mins, and 30 mins. Schematic illustrations of director profiles for (b) planar and (c) homeotropic orientations of 5CB on TiO_2(101).

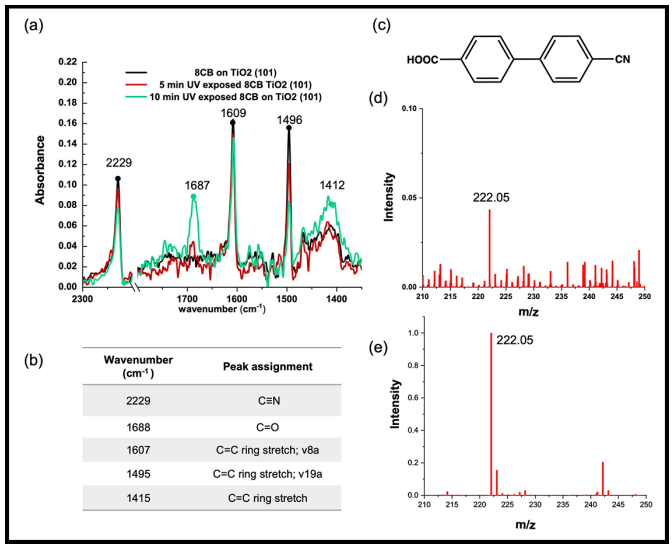

Figure 3: (a) PMIRRAS spectra of nanometer-thick layers of 8CB on TiO_2(101) (black), exposed to 365 nm UV illumination for 5 mins (red) and 10 mins (green). (b) Vibrational frequency (cm^{-1}) assignments for peaks in (a) ν represents stretching, and β represents in-plane bending. (c) Molecular structure of 4'-cyanobiphenyl-4-carboxylic acid (CBCA). Electrospray ionization-mass spectra plot of (d) 25 µM 5CB reacted under 365 nm UV illumination on TiO_2(101) (e) 5 µM CBCA in methanol collected in negative ionization mode.

at 80% RH (Figure 1(c), (e), (f)). Prior studies have reported that water can adsorb to metal oxides such as titania under ambient humidity conditions and that the surface coverage of water is dependent on the humidity level [2]. Ongoing experiments are testing the hypothesis that increasing water coverage on TiO_2(101) weakens the binding of 5CB in the perpendicular mode and triggers an orientational transition.

To study the influence of the photocatalytic activity of TiO_2(101) on the orientations of nematic 5CB, we illuminated micrometer-thick films of 5CB on TiO_2(101) at a wavelength of 365 nm under 80% RH. Upon UV illumination, the optical appearance of the nematic 5CB film changed from bright to dark, indicating an orientational transition from planar to homeotropic as shown in Figure 2(a), (b). In contrast, no change in optical appearance was observed when a micrometer-thick film of 5CB supported on a photo-inactive silica surface was illuminated with UV light. Additional support for our conclusion that the orientational transition of 5CB observed on TiO_2(101) was driven by photocatalytic activity was obtained by using PMIRRAS measurements of nanometer-thin films of 8CB (a homolog of 5CB) supported on TiO_2(101) on platinum-coated Si wafers. Platinum films were e-beam deposited on Si wafers. Upon UV illumination, we measured a new peak in the IR spectrum corresponding to a C=O group (1688 cm^{-1}), consistent with photo-oxidation of 8CB to a carbonyl-containing compound as indicated in Figure 3 (a), (b). Mass-spectrometry confirmed that photo-oxidation of 5CB on TiO_2(101) forms the acid-containing molecule 4'- cyanobiphenyl-4-carboxylic acid (CBCA) (structure shown in Figure 3(c)) as indicated in Figure 3(d), (e).

Prior studies have revealed that carboxylic acid-containing molecules bind strongly to titania in the perpendicular mode [1]. This prior result provides support for our conclusion that the photocatalytic activity of TiO_2(101) can generate a carboxylic acid-containing compound within a nematic film of 5CB and thus trigger homeotropic anchoring of the LC mixture. This result provides the first evidence that photocatalytic transformations on titania can be coupled to orientational transitions in LCs.

Current work in this project is focused on understanding how the ligand environment created by a LC can modify the catalytic activity of titania.

References:

[1] Nanqi Bao, Jake I. Gold, Jonathan K. Sheavly, James J. Schauer, Victor M. Zavala, Reid C. Van Lehn, Manos Mavrikakis, and Nicholas L. Abbott, Ordering Transitions of Liquid Crystals Triggered by Metal Oxide-catalyzed Reactions of Sulfur Oxide Species. J. Am. Chem. Soc. 2022, 144, 36, 16378-16388. https://pubs.acs.org/doi/full/10.1021/jacs.2c03424

[2] A. L. Goodman, E. T. Bernard, and V. H. Grassian, Spectroscopic Study of Nitric Acid and Water Adsorption on Oxide Particles: Enhanced Nitric Acid Uptake Kinetics in the Presence of Adsorbed Water. J. Phys. Chem. A 2001, 105, 6443-6457. https://pubs.acs.org/doi/abs/10.1021/jp003722l

Investigation of Dry Chemical Actuators using Palladium and Palladium-Gold Thin Films

CNF Project Number: 2736-18
Principal Investigator(s): Nicholas Lawrence Abbott[1]
User(s): Hanyu Alice Zhang[2]

Affiliation(s): 1. Smith School of Chemical and Biomolecular Engineering, Cornell University, Ithaca NY, USA; 2. School of Applied and Engineering Physics, Cornell University, Ithaca NY, USA

Primary Source(s) of Research Funding: Cornell Center for Materials Research with funding from the National Science Foundation Materials Research Science and Engineering Centers program (DMR-1719875)

Contact: nla34@cornell.edu, hz496@cornell.edu

Website(s): https://nlabbottcornell.weebly.com/

Primary CNF Tools Used: Heidelberg DWL2000 Mask Writer, ABM Contact Aligner, Oxford 81/82/100 Etchers, AJA Sputter Deposition Tool, Oxford PECVD, Plasma-Therm Takachi HDP-CVD, SC4500 Odd-Hour Evaporator, Plasma-Therm 770 Etcher (Left Side), OEM Endeavor Aluminum Nitride Sputtering System, Leica CPD300, DISCO Dicing Saw

Abstract:

This project is focused on the fabrication of chemical actuators from palladium or palladium-gold thin films and characterization of their actuation using hydrogen gas. Previously, we reported on the design of chemical actuators using surface reactions on platinum thin films [1]. In contrast to platinum, atomic hydrogen can diffuse into palladium and palladium-gold thin films, thus generating strains and stresses that are larger than those that can be realized using surface reactions of platinum. In this report, we describe our results with palladium actuators, as well as present some initial results with the palladium-gold bimetallic system.

Summary of Research:

We are exploring how palladium can be used in microscopic bimorph structures that function as chemically-driven hinges. The work is motivated by prior studies of the dissociation of hydrogen on the surface of palladium and diffusion of atomic hydrogen into the palladium lattice to trigger a phase transition [2].

The goal of this project is to harness the bulk absorption of atomic hydrogen into palladium and the subsequent phase transition to drive actuation on the microscale. By fabricating bilayers of palladium and titanium (equal in thickness), we have shown that it is possible to selectively strain one half of the device relative to the other half thus generating a bending of the bimorph. Preliminary results hint that the actuation dynamics are influenced by a first-order phase transition upon exposure to hydrogen gas.

In addition to palladium, we have also started fabricating actuators using a palladium-gold bimetallic system due to its ability to surpass the first order phase transition and undergo a second-order phase transition beyond a certain gold concentration in the alloy. We predict that the order of the phase transition will be reflected in the dynamics of the actuator response [3].

To accomplish this goal, we purchased palladium sputtering targets for CNF and are co-sputtering palladium and gold. Pure sputtered palladium grains were first characterized with a scanning electron microscope as seen in Figure 1, and the smallest possible grain size (obtained by sputtering at 3mTorr) was chosen to build actuators.

To fabricate these devices, a sacrificial layer of aluminum nitride is sputtered onto a fused silica wafer with the OEM Endeavor sputtering system and a layer of aluminum oxide is grown with the Oxford FlexAl on top of the aluminum nitride. Both layers are then patterned and etched in the PT770. After the aluminum nitride is etched, a layer of silicon dioxide is grown with plasma enhanced chemical vapor deposition (PECVD) or high density plasma chemical vapor deposition (HPD-CVD) techniques and patterned. Finally, the bimorph microactuator consisting of titanium and either palladium or palladium-gold is sputtered onto the chip and patterned via lift-off. After the devices are fully fabricated, the chip is soaked in MIF 726 overnight to etch away the aluminum nitride and aluminum oxide layers. It is then dried in the Leica critical point dryer. The chips are then moved to a custom-built exposure chamber for testing in different gaseous environments.

Conclusions and Future Steps:

We have fabricated hinges that show a repeatable actuation upon the application of hydrogen, as shown in Figure 2.

In addition, initial results with palladium-gold show that the alloy responds faster than the pure metal under hydrogen exposure, as shown in Figure 3.

In the future, we aim to characterize further the phase transitions that occurs when palladium is exposed to hydrogen and the influence of the phase transitions on actuation dynamics. Additionally, we will characterize a wider range of compositions of palladium-gold to develop an understanding of how changes in the order of the phase transitions impacts actuator performance.

References:

[1] Nanqi Bao, et al. Gas-phase microactuation using kinetically controlled surface states of ultra-thin catalytic sheets. PNAS, 120(19), 2023.

[2] Noah J. J. Johnson, et al. Facets and vertices regulate hydrogen uptake and release in palladium nanocrystals. Nature materials, 18(5), 2019.

[3] A. Maeland, and T.B Flanagan. X-ray and thermodynamic studies of the absorption of hydrogen by gold-palladium alloys. The Journal of Physical Chemistry, 69(10), 1965.

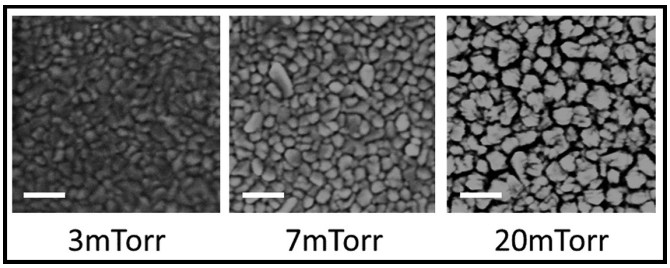

Figure 1: SEM images of grain structures of palladium films sputtered at 3, 7, and 20 mTorr. Scale bars are 100 nm.

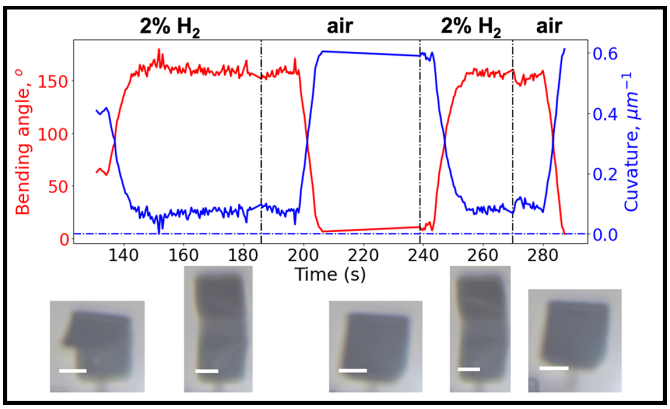

Figure 2: Single palladium hinge (bimorph) responding to hydrogen and air. Scale bars are 5 μm.

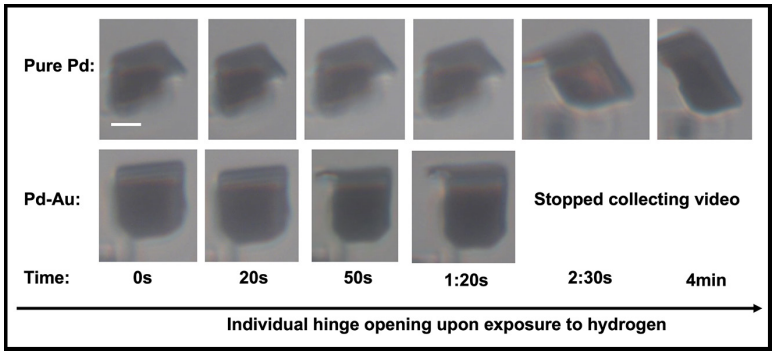

Figure 3: Comparison of responses of actuators fabricated from palladium versus a 24% palladium-gold alloy. Scale bar is 5 μm.

Auto-Fluorescent Polymer Brushes for Glucose Detection

CNF Project Number: 2751-18
Principal Investigator(s): Christopher Kemper Ober
User(s): Gozde Aktas Eken

Affiliation(s): Department of Material Science and Engineering, Cornell University
Primary Source(s) of Research Funding: National Science Foundation
Contact: cko3@cornell.edu, ga352@cornell.edu
Website(s): https://ober.mse.cornell.edu/
Primary CNF Tools Used: E-beam Resist Spinners, JEOL 9500, Oxford 81, Zeiss Ultra SEM, Optical Microscope

Abstract:

Polymer brushes possess considerable potential for designing smart surfaces suited for a diverse range of applications, such as controlled cell adhesion, self-cleaning surfaces, and smart actuators. Introduction of luminescent properties to polymer brushes has facilitated novel characterization techniques and opened up new applications in sensing and optoelectronics. In this study, we introduce a fluorescent glucose sensing platform that utilizes auto-fluorescent copolymer brushes functionalized with phenylboronic acid (PBA). These brushes exhibit conformational changes upon binding with glucose, leading to alteration in aggregation-induced emission (AIE). An integrated process involving electron-beam lithography, surface-initiated polymerization, and post-polymerization modification was employed to create nanopatterned polymer brushes.

Summary of Research:

Smart polymeric materials that exhibit prompt feedback when exposed to external stimuli hold great potential, particularly in biomedical field. These materials find applications in drug delivery, sensing, and diagnostics [1]. Consequently, the development of smart (bio) interfaces capable of sensing and responding to changes in the local environment presents intriguing possibilities for surface-based sensing concepts [2]. Polymer brushes are highly suitable for designing adaptive and responsive interfaces due to their diverse range of functional and structural options. Notably, these thin polymeric coatings offer rapid response times while minimally affecting the physical properties of the underlying cores or substrates [3]. By integrating these systems with sensing and reporting entities, such as colorimetric or luminescent components, efficient transduction mechanisms can be achieved [4].

Previously, we demonstrated that polymer brushes built from AIE polymers can generate optical signals from pH-induced conformational changes without conventional fluorophores [5]. In this work, we extend the application of AIE polymers to design glucose responsive surfaces by combining auto-fluorescent poly(styrene-*alt*-maleic anhydride) (pSMA) copolymer brushes with boronic acid receptors. This work builds on the nanopatterning process reported earlier [6]. Preparation of boronic acid containing pSMA brushes was achieved via an integrated fabrication process of area-selective deposition of initiator, surface-initiated polymerization, and post-polymerization modification (PPM). Polymer brushes were grown from both patterned and non-patterned substrates.

E-Beam Resist Mask Preparation. E-beam resist was patterned via JEOL 9500, which was later used as the mask for the vapor deposition of silane coupling agent. Prior to the deposition, the substrate was descummed via the Oxford 81 etcher to remove residual debris in the unmasked area.

Initiator Immobilization. The vapor deposition of the silane coupling agent was carried out in a closed chamber at 1 torr and 70°C for 18 hours. The substrate was cleaned with organic solvents to remove the resist mask and then transferred into a sealed flask with a solution of azo-initiator. The immersion time was 24 hours.

Brush Synthesis and Modification. Polymer brushes were synthesized via surface-initiated radical polymerization in acetonitrile at 85°C, using equimolar amounts of styrene and maleic anhydride. PPM with 3-aminophenylboronic acid with was conducted at room temperature and the degree of functionalization was adjusted through the reaction time.

Characterization and Results:

The patterned e-beam resist was characterized using Zeiss Ultra scanning electron microscopy. Patterned

brushes, thickness and morphology of non-patterned samples were analyzed by atomic force microscopy (AFM) after each step using the Asylum Research Cypher ES (Figure 1). The fluorescence characteristics and the response of the brushes to changes in pH and glucose levels were monitored using two-photon confocal microscopy (Zeiss LSM i880) (Figure 2). Fluorescence images were scanned in λ mode from 413 to 693 nm (λex = 800 nm) and the corresponding emission spectra were generated through 64 spectral sections. Figure 3 illustrates the changes in emission intensity observed when brushes were subjected to the buffer solutions with varying glucose concentrations. An increase in glucose concentration led to a substantial change in fluorescence intensity, wherein the increase in brush height from 136 to 460 nm corresponded to 83% decrease in fluorescence intensity. The steep decline in fluorescence intensity is attributed to the hydration and highly extended conformation of the polymer chains. In this state, the intra- and interchain interactions are constrained, limiting cluster formation, and subsequently affecting the fluorescence properties.

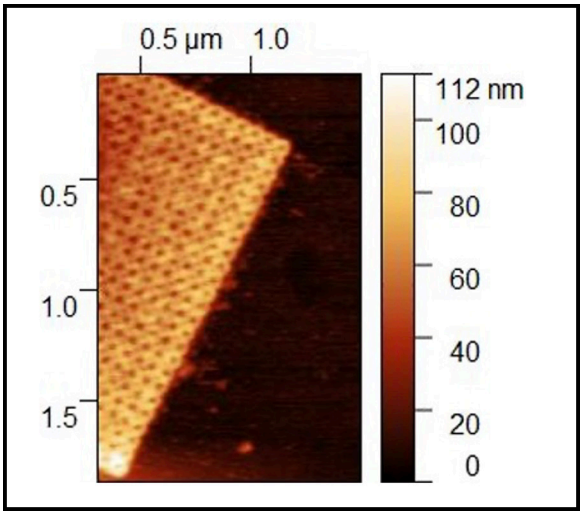

Figure 1: AFM height image of patterned pSMA brushes.

Conclusions and Future Steps:

Glucose responsive luminescent surfaces were prepared through an integrated process involving electron-beam lithography, surface-initiated polymerization, and post-polymerization modification. Utilizing auto-fluorescent polymer brushes, we have successfully demonstrated their ability to translate conformational transitions, triggered by binding events, into fluorescent readouts. Our primary objective is to optimize both sensitivity and pH parameters, thereby obtaining polymer brushes capable of operating within the physiologically relevant range.

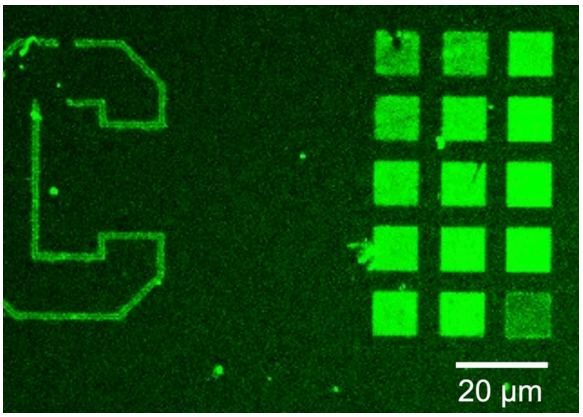

Figure 2: Confocal laser scanning microscopy images of the patterned brushes in collapsed state (pH 3).

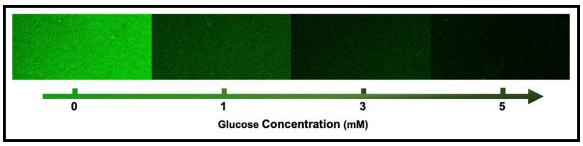

Figure 3: Confocal laser scanning microscopy images of brushes captured in solutions with varying glucose concentrations (pH 9).

References:

[1] Wei, M.; Gao, Y.; Li, X.; Serpe, M. J., Stimuli-responsive polymers and their applications. Polym Chem-Uk 2017, 8 (1), 127-143.

[2] Chen, W.-L.; Cordero, R.; Tran, H.; Ober, C. K., 50th Anniversary Perspective: Polymer Brushes: Novel Surfaces for Future Materials. Macromolecules 2017, 50 (11), 4089-4113.

[3] Li, D.; Xu, L.; Wang, J.; Gautrot, J. E., Responsive Polymer Brush Design and Emerging Applications for Nanotheranostics. Advanced Healthcare Materials 2021, 10 (5), 2000953.

[4] Poisson, J.; Hudson, Z. M., Luminescent Surface-Tethered Polymer Brush Materials. Chemistry - A European Journal 2022, 28 (32), e202200552.

[5] Aktas Eken, G.; Huang, Y.; Guo, Y.; Ober, C., Visualization of the pH Response through Autofluorescent Poly(styrene-alt-N-maleimide) Polyelectrolyte Brushes. ACS Applied Polymer Materials 2023, 5 (2), 1613-1623.

[6] Huang, Y.; Tran, H.; Ober, C. K., High-Resolution Nanopatterning of Free-Standing, Self-Supported Helical Polypeptide Rod Brushes via Electron Beam Lithography. ACS Macro Letters 2021, 10 (6), 755-759.

Fluorination Effect on Anti-Penetration Performance of Polystyrene-*Block*-Poly(vinylmethylsiloxane)

CNF Project Number: 2751-18
Principal Investigator(s): Christopher Kemper Ober
User(s): Zhenglin Zhang

Affiliation(s): Department of Material Science and Engineering, Cornell University

Primary Source(s) of Research Funding: Defense Threat Reduction Agency

Contact: cko3@cornell.edu, zz288@cornell.edu
Website(s): https://ober.mse.cornell.edu/

Primary CNF Tools Used: YES LP-III vacuum oven, Photolithography Spinners, DISCO Dicing Saw, Jelight 144AX UVO-Cleaner, Veeco Icon AFM, Woollam RC 2 Ellipsometer

Abstract:

A series of fluorinated polystyrene-*block*-poly(vinylmethylsiloxane) (PS-*b*-PVMS) polymers were synthesized by anionic polymerizations and thiol-ene reactions. The synthesized fluorinated PS-*b*-PVMS polymers were further characterized by nuclear magnetic resonance (NMR), differential scanning calorimetry (DSC), and small-angle X-ray scattering (SAXS). The introduction of fluorine can enhance intra and intermolecular interactions, which limit the flexibility of polymer chains and improve polymers' anti-penetration performance.

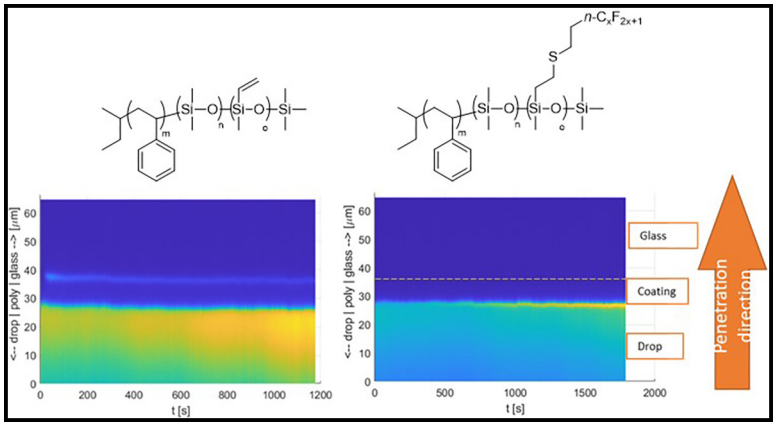

*Figure 1: Anti-penetration performance of nonfluorinated PS-*b*-PVMS (left) and fluorinated PS- PS-*b*-PVMS (right).*

Summary of Research:

Polydimethylsiloxane (PDMS) based surface coating materials are widely explored in antifouling and fouling release materials for marine vessels, as PDMS has low surface energy and elastic modulus, and is chemically stable and eco-friendly. Current research is highly focused on modifying PDMS with different functional groups to tune surface hydrophobicity, hydrophilicity, and amphiphilicity to adjust polymers' antifouling and fouling release performance on the surface [1].

Although fouler or contamination on the surface can be cleaned by water jet, the contamination just under the surface would be a problem that may damage the exposed surface performance and durability, as PDMS is a flexible backbone with nano-sized intermolecular spaces (free volume) and molecular level penetration into PDMS films can occur [2]. The introduction of fluorine is supposed to increase inter/intramolecular interactions [3], and is able to limit polymers' flexibility and movability of the free volume, which should restrict penetration theoretically.

In this research, a series of fluorinated alkyl chains with different lengths are attached to PVMS by thiol-ene click reaction to explore the fluorination effect on the penetration of PDMS.

NMR spectra show that the chemical shifts of fluorine shift to upfield and the chemical shifts of silicon shift to downfield after the fluorinated alkyl chains were grafted to PS-*b*-PVMS backbone, which indicates interactions between fluorine atoms and silicon atoms, as electron acceptors and donors, respectively. DSC results show that the glass transition temperature (T_g) for the PVMS block increases with the length of the fluorinated alkyl chain. SAXS results show that more ordered patterns of hexagonal columns can be observed after the fluorination. Fluorinated PS-*b*-PVMS polymers were dissolved, and spin-coated on glass slides, which were cleaned, and processed by YES LP-III vacuum oven. The test of contact angles of the films shows that fluorination increased the contract angle (water) from 92° of the nonfluorinated precursor to 111°. Penetration

tests on films of fluorinated PS-*b*-PVMS were recorded by a laser confocal microscope with aqueous solutions of Rhodamine B as a dye, which showed that fluorination can effectively improve the anti-penetration performance of PS-*b*-PVMS (see Figure 1).

Conclusions:

Our current results support that the introduction of fluorine in PS-*b*-PDMS enhances intra/intermolecular interactions, which can restrict the movements of free volumes in PVMS and improve its anti-penetration performance.

References:

[1] Leonardi, A. K.; Ober, C. K. Annu. Rev. Chem. Biomol. Eng. 2019, 10, 241.264.

[2] Saito, M.; Nishimura, T.; Sakiyama, K.; Inagaki, S. AIP Adv. 2012, 2, 042118.

[3] Kim, S.; Saxena, A.; Kwak, G.; Fujiki, M.; Kawakami, Y. Chem. Commun. 2004, 538.539.

Design, Synthesis, and Multiscale Structural Investigation of Polymer-Grafted Nanoparticles (PGNs) for Application in Pyrolysis and Self-Assembly Processes

CNF Project Number: 2955-21
Principal Investigator(s): Christopher Kemper Ober
User(s): Chenyun Yuan

Affiliation(s): Department of Materials Science and Engineering, Cornell University
Primary Source(s) of Research Funding: Air Force Office of Scientific Research (AFOSR)
Contact: cko3@cornell.edu, cy479@cornell.edu
Primary CNF Tools Used: Malvern Nano ZS Zetasizer, Dicing Saw, Zeiss Ultra SEM

Abstract:

The research team has made extensive strides in the study of polymer-grafted nanoparticles (PGNs) over the past year, utilizing the top-tier resources and support from the Cornell NanoScale Facility (CNF) as well as other facilities on campus. Two critical aspects of PGNs — self-assembly and pyrolysis to make polymer-derived ceramics (PDCs) — were investigated, providing key insights into how grafting density influences self-assembly and how varying pyrolysis conditions can tailor PGN-derived inorganic nanostructured materials. Our findings have the potential to transform various applications, including optical devices, magnetic devices, catalysis, energy storage, and the broader field of materials science.

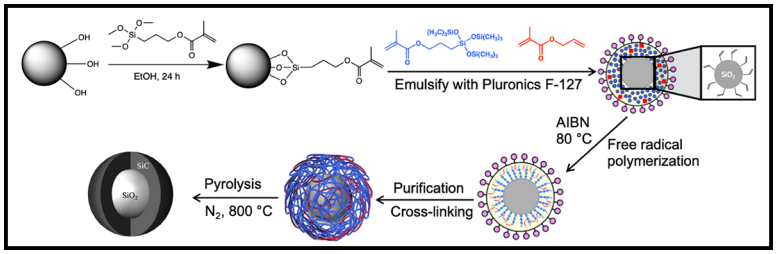

Figure 1: "Grafting-through" approach in mini-emulsion to covalently attach preceramic polymer chains to the silica surface, crosslinking of the preceramic polymer brushes via the allyl groups, and pyrolyze the PGNs to get SiO_2-SiC core-shell nanoparticles.

Summary of Research:

Synthesis, Functionalization and Self-Assembly of Polymer-Grafted Nanoparticles (PGNs). Our research began with the robust synthesis of PGNs with varied grafting densities [1]. A modified initiator, APTES-BIBB, was employed to functionalize silica nanoparticles (Ludox TM-40), which were then grafted with different polymers containing either hydrogen bonding donors or acceptors to create the PGNs. This process was optimized through iterative testing to yield PGNs with a range of grafting densities, thus enabling us to explore their impacts on self-assembly.

Utilizing transmission electron microscopy (TEM) and scanning transmission electron microscopy (STEM), we analyzed the PGNs' self-assembly behaviors. Our research established a direct link between the grafting density and self-assembly behavior of PGNs. This has opened a gateway to the predictable design of PGNs, enabling a more refined approach to their utilization in fields such as nanoparticle-based optical devices.

Pyrolysis of PGNs. In our other piece of work, we delved into the pyrolysis of preceramic polymer-grafted nanoparticles and its implications (Figure 1). Our objective was to understand how synthesis and pyrolysis conditions, impact the resultant structure, morphology, and composition of the preceramic PGN-derived nanostructured materials. CNF's state-of-the-art facilities enabled in-depth analysis and characterization of the outcomes.

Our findings, derived from thermogravimetric analysis, Fourier-transform infrared spectroscopy, scanning electron microscope (SEM) and high-resolution TEM, indicated that PGNs' pyrolysis led to the creation of SiO_2-SiC core-shell nanomaterials.

Future Plans:

Our groundbreaking progress over the past year paves the way for ambitious future research. We are particularly interested in investigating the influence of polymer chemistry on both the self-assembly behavior and pyrolysis outcomes of PGNs.

CNF's state-of-the-art facilities will enable us to take a deep dive into the structures derived from PGNs assembly and pyrolysis. Additionally, we're planning to focus our efforts on uncovering new applications of PGNs in areas such as optical and magnetic devices, as well as polymer-derived ceramic nanostructures.

References:

[1] Yuan, C., Käfer, F., and Ober, C. K. (2021). Polymer-Grafted Nanoparticles (PGNs) with Adjustable Graft-Density and Interparticle Hydrogen Bonding Interaction. Macromolecular Rapid Communications, 43(12), 2100629. https://doi.org/10.1002/marc.202100629

Imaging the TaS_2 Charge Density Wave Transition in Real-Space with Electron Microscopy

CNF Project Number: 2967-21
Principal Investigator(s): Jeeyoung Judy Cha
User(s): James L. Hart, Saif Siddique

Affiliation(s): Department of Materials Science and Engineering, Cornell University

Primary Source(s) of Research Funding: Gordon and Betty Moore Foundation, EPiQS Synthesis Investigator Award

Contact: jc476@cornell.edu, jlh478@cornell.edu, ms2895@cornell.edu

Website(s): cha.mse.cornell.edu

Primary CNF Tools Used: CHA evaporator, Zeiss Supra scanning electron microscope, Nabity system for Supra

Abstract:

We studied the charge density wave (CDW) and insulator-to-metal transition in the two-dimensional (2D) material tantalum(IV) sulfide (TaS_2). We highlight two key findings: first, basal dislocations strongly influence the transition, acting as both nucleation and pinning sites, and second, the bias-induced CDW switching is driven by Joule heating. Both findings are relevant to the design of next-generation electronics based on TaS_2.

Summary of Research:

Tantalum(IV) sulfide (TaS_2) is a prototypical 2D quantum material that hosts several CDW phases. At low temperature, the TaS_2 ground state is the commensurate (C) CDW phase, which is insulating [1]. Above 200 K, TaS_2 transitions to the nearly commensurate (NC) CDW phase, which is defined by a network of phase slips in the CDW order parameter, i.e. discommensurations [1]. The NC phase is metallic. Hence, the C to NC phase transition is accompanied by a large change in electrical resistance, and is promising for device applications. Moreover, the transition can be triggered with an applied electric field, with potential application for 2-terminal devices [2]. However, implementing nanoscale TaS_2 devices requires a detailed understanding of how the CDW phase transition occurs on nanoscale dimensions, which is currently lacking. Direct real-space imaging of the CDW transition is needed.

We developed a four-dimensional scanning transmission electron microscopy (4D-STEM) approach which allows the visualization of the CDW transition. In 4D-STEM, an electron beam is focused to a nanoscale probe, rastered across the sample surface, and a full diffraction pattern is captured at each spatial coordinate [3]. Our method provides significant advantages over prior attempts to image the CDW transition [4,5].

Figure 1 shows the resistance versus temperature for a TaS_2 device measured within the electron microscope. A clear insulator-to-metal transition is observed around ~ 200 K. For each of the datapoints in Figure 1, a full 4D-STEM dataset was collected and used to map out the CDW phase; select temperature scans are shown in Figure 2. For the C to NC CDW transition, the appropriate order parameter is the coherent domain size DNC. At 120 K in the insulating phase, the measured domain size DNC is > 100 nm, which is consistent with the C CDW phase. At 250 K, in the metallic phase, the DNC is < 10 nm, consistent with the NC CDW phase. Interestingly, at the insulator-to-metal transition (195 K), we find that the DNC map displays sharp lines and domains. Hence, the CDW transition is highly inhomogeneous.

To understand the nature of the sharp lines seen in the CDW map, we performed additional electron microscopy experiments. We find that all of the lines seen in the CDW map correspond to basal dislocations, i.e. both the burgers vector and the line vector lie in the ab-plane. A plan-view STEM image of one such dislocation is shown in Figure 3. We find that dislocations both nucleate and pin the CDW transition in TaS_2, thus, device engineering efforts should consider the role of dislocations.

Next, we investigate electric field-induced switching of TaS_2. Nearly a decade ago, several research groups showed that starting in the insulating C phase, application of a strong electric field can trigger a rapid transition to a metallic phase. The switching is fast, reversible, and energy-efficient, making this switching process appealing for 2-terminal devices [2]. However, the actual switching mechanism is still under debate.

To resolve this question, we operate a 2-terminal device within the electron microscope. In doing so, we can image the CDW during device operation, offering unprecedented insight to the switching process. Here, we

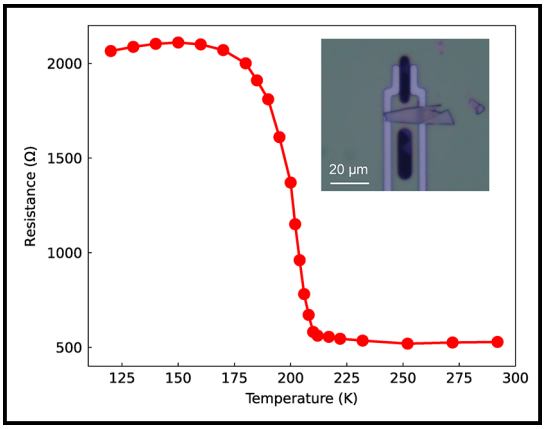

Figure 1: In situ *STEM resistance versus temperature for a TaS_2 device upon heating. Inset shows optical image of device.*

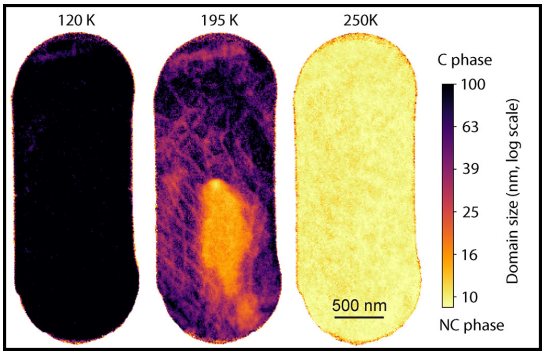

Figure 2: Select 4D-STEM maps of the CDW order parameter, captured simultaneous with the resistance data in Figure 1.

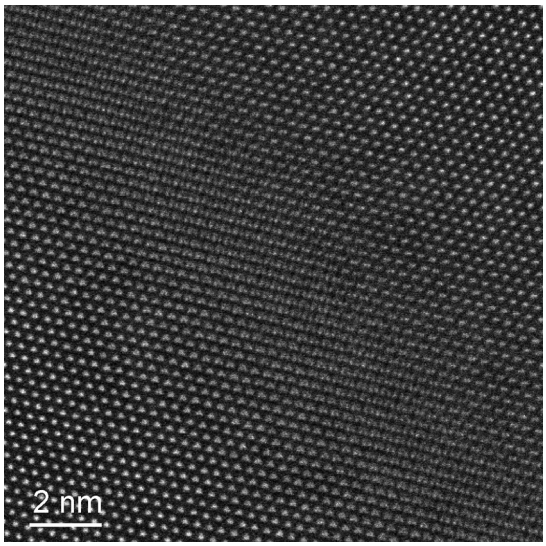

Figure 3: Atomic-resolution STEM image of a basal dislocation, imaged in the ab-plane. The dislocation line runs from the top-left to the bottom-right of the image.

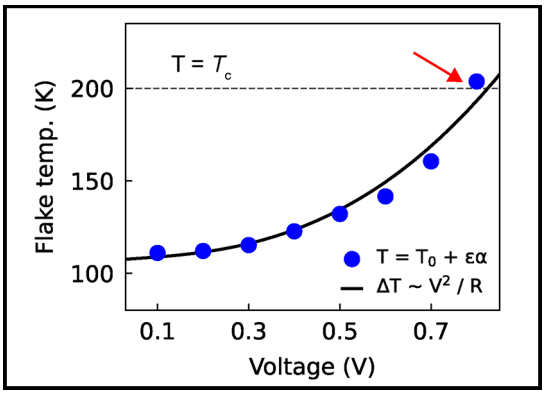

Figure 4: The measured flake temperature versus applied voltage. Resistive switching occurs when the temperature surpasses the CDW transition temperature T_c (red arrow).

highlight one key finding from these experiments, which proves that switching is driven by Joule heating. First, we apply a DC voltage to our flake, while simultaneously measuring the flake resistance and collecting diffraction data. From the diffraction data, we extract the flake strain, and using the thermal coefficient of expansion, we can then determine the flake temperature. Figure 4 shows the measured flake temperature as a function of applied voltage. For voltages from 0.1 to 0.7 V, the flake is highly resistive (> 2 kΩ). Then, at 0.8 V, the resistance drops to 400 Ω. At the resistive transition, we see that the flake temperature surpasses 200 K, which is the thermal transition point for the TaS_2 C to NC phase transition. Hence, our data shows that at the critical voltage which causes resistive switching, the Joule heating is sufficient to raise the flake temperature above the CDW transition temperature.

Conclusions:

We used in operando 4D-STEM to study the CDW behavior of the 2D quantum material TaS_2. We showed that dislocations both nucleate and pin the CDW transition, and that the bias-induced transition is driven by Joule heating. These findings are important for the optimization of next-generation TaS_2 devices.

References:

[1] Ishiguro, T., and Sato, H. Phys. Rev. B 44, 2046-2060 (1991).
[2] Vaskivskyi, I., et al. Nat. Commun. 7, 11442 (2016).
[3] Ophus, C. Microsc. Microanal. 25, 563-582 (2019).
[4] Frenzel, A. J., et al. Phys. Rev. B 97, 035111 (2018).
[5] Walker, S. M. et al. Nano Lett. 22, 1929-1936 (2022).

Photolithographic Patterning of Alignment Fiducials for X-Ray Nano-Diffraction

CNF Project Number: 2989-21
Principal Investigator(s): Andrej Singer
User(s): Aileen Luo, Saptarshi Das

Affiliation(s): Materials Science and Engineering, Cornell University

Primary Source(s) of Research Funding: National Science Foundation, Department of Energy

Contact: asinger@cornell.edu, al2493@cornell.edu, sd724@cornell.edu
Website(s): https://singer.mse.cornell.edu/

Primary CNF Tools Used: Heidelberg Mask Writer - DWL2000, Hamatech Mask Chrome Etch, ABM Contact Aligner

Abstract:

Alkaline fuel cells and electrolyzer cells are promising alternative forms of energy conversion and storage devices due to their potential for eliminating the need for precious-metal catalysts. Epitaxially grown transition metal oxide thin films have demonstrated promising activity for the oxygen reduction reaction [1], the rate-limiting step for catalysis in alkaline fuel cells. To better understand localized structural and electronic changes in the catalyst under operating conditions, we aim to study them using x-ray nano-diffraction and x-ray absorption near-edge structure at the hard x-ray nanoprobe beamline at the National Synchrotron Light Source II.

Summary of Research:

Focusing of x-rays to a 25 nm spot on a sample requires alignment fiducial markers with sharp edges of less than half a micron in width. Using the computer-aided design software L-Edit and the Heidelberg Mask Writer - DWL2000, we designed and wrote a 5-inch photomask with multiple configurations of the pattern shown in Figure 1. Using S1800 series positive tone photoresist and the ABM Contact Aligner, we transferred the pattern onto samples of sizes 5 mm × 5 mm and 10 mm × 10 mm. DC magnetron sputtering (Cornell Center for Materials Research) was used to deposit 10 nm of titanium and 50 nm of copper metal onto the samples. Sonication in acetone was used to lift off the excess metal and complete the process.

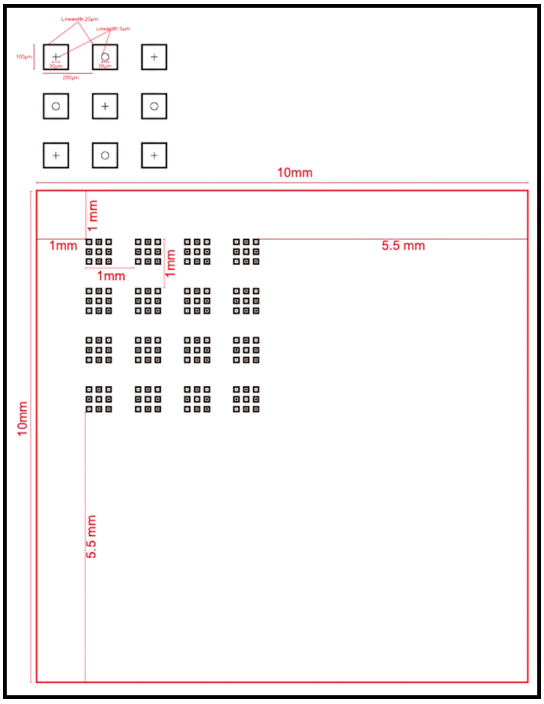

Figure 1: Schematic credit to Dr. Ludi Miao. Arrays of circles and crosses contained in larger squares.

Conclusions and Future Steps:

The fabrication of alignment features was completed successfully and tested at the hard x-ray nanoprobe beamline. For future measurements, we will design and make proof-of-concept devices at the Cornell NanoScale Facility (CNF) for a three-electrode electrochemical cell compatible with the limitations of the beamline. Prior work that used CNF tools was published and presented as detailed below.

Publication:
https://doi.org/10.1063/5.0125268

Conference presentation, 2022 Materials Research Society (MRS) Fall Meeting: Title: "X-ray Nano-Imaging of Defects in Thin-Film Catalysts via Cluster Analysis."

References:

[1] Y. Yang, et al. J. Am. Chem. Soc. 2019, 141, 1463-1466.

Quasi-2D Materials for Ultra-Low Resistance Electrical Interconnects

CNF Project Number: 3007-22
Principal Investigator(s): Hair P. Nair
User(s): Bilal Azhar, Cameron Gorsak

Affiliation(s): Department of Materials Science and Engineering, Cornell University

Primary Source(s) of Research Funding: Semiconductor Research Corporation (SRC)

Contact: hn277@cornell.edu, ba428@cornell.edu, cag284@cornell.edu

Primary CNF Tools Used: General Materials Anneal Furnace, Veeco Savannah ALD, Woollam RC2 Spectroscopic Ellipsometer, AFM -Veeco Icon

Abstract:

The dramatic increase in the resistivity of interconnect lines with decreasing dimensions presents a significant bottleneck for further downscaling of integrated circuits [1]. This is because current interconnects use 3-dimensional metals that experience increased interface electron scattering as the interconnect dimensions approach their electron mean free path. A possible solution is to use metals with much lower electron mean free paths such as: W, Mo, and Ru. Metallic delafossite oxides are an alternative solution because of their inherent advantages over traditional metals such as: ultra-low room temperature resistivity, potential mitigation of interface/surface scattering due to their 2D Fermi surface, potentially decreased likelihood of electromigration, and potentially better compatibility with low-κ oxide dielectrics. Metallic delafossite can prove to be a disruptive new material for ultra-scaled electrical interconnects.

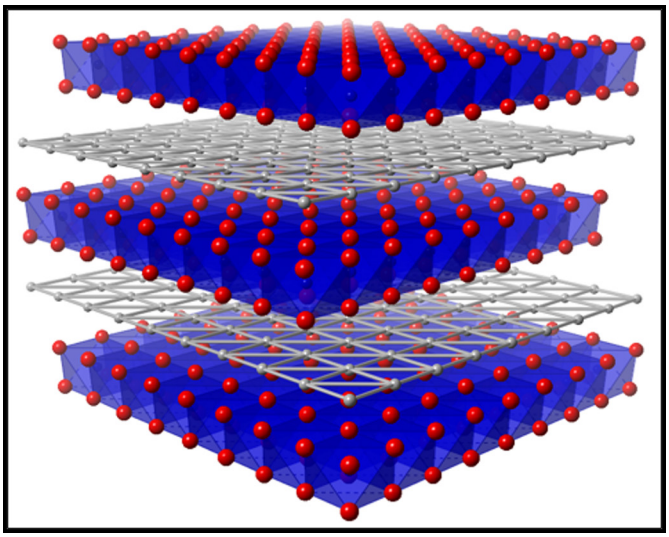

Figure 1: Crystal structure of delafossite PtCoO2 illustrating the sheets of Pt responsible for the anisotropic conductivity.

Introduction:

Delafossites are layered oxides with the formula ABO_2 where A is a metal cation that forms 2D sheets separated by the BO_2 transition-metal oxide octahedra, Figure 1. In this study we focus on metallic delafossites $PtCoO_2$ and $PdCoO_2$ because of their ultra-low room temperature resistivity of 2.1 $\mu\Omega$.cm and 2.6 $\mu\Omega$.cm, respectively, which is comparable to the current semiconductor industry standard interconnect metal, Cu, Figure 2 [2]. The metallic delafossite structure has an anisotropic nature with resistivity along the c-axis a factor of 1000 higher than resistivity within the Pt/Pd sheet. Due to the layered crystal structure, the Fermi surface of the metallic delafossites is cylindrical as for a 2D metal. This quasi-2D crystal structure can potentially mitigate interface and surface scattering since the electron Fermi velocity does not have components perpendicular to the Pd/Pt sheets. This can potentially overcome the resistivity penalty encountered by conventional 3D metals in ultrathin films (< 20 nm). Additionally, the unique Fermi surface topology allows for an electron-phonon coupling constant that is a factor of 3 lower than copper [3].

Our focus has been to demonstrate metallic delafossites as a disruptive new material for ultra-scaled electrical interconnects, for which we have two goals. The first goal is to realize their unique electrical properties and the second goal is to demonstrate the growth of highly quality delafossite thin films via atomic layer deposition (ALD) a back-end-of-the-line (BEOL) compatible synthesis technique.

Summary of Research:

To realize the unique electrical properties of delafossite thin films we have been investigating the structural and electrical properties of $PdCoO_2$ thin films grown via molecular beam epitaxy (MBE). MBE has been shown to achieve highly crystalline films which is critical for electrical property characterization due to the structure-property relation [4,5]. We used high-resolution X-Ray diffraction (HRXRD) to confirm that the films are phase-pure. We measured the resistivity of the films using a van der Pauw geometry and modelled the resistivity scaling with film thickness using Fuchs-Sondheimer (FS) and Mayadas-Shatzkes (MS) model. The upshot being that a 50 nm thick $PdCoO_2$ film has a resistivity of 5 $\mu\Omega$.cm. It should be noted that while our XRD phi scans did reveal in-plane twinning our resistivity fitting did not find twin boundaries to be a significant contributor to resistivity.

We have also combined thermodynamic modelling with *ex-situ* annealing to characterize the amorphous to crystalline transition in molecular beam epitaxy (MBE) grown $PdCoO_2$ thin films. This characterization was very insightful in finding the relevant temperature range and secondar phases. This characterization allows us to transition from MBE to BEOL-compatible ALD which typically deposits amorphous films. This complements our ALD growth $PtCoO_2$ thin films for which we are currently calibrating the Co_xO_y and PtO binary cycles to later combine into the $PtCoO_2$ supercycle.

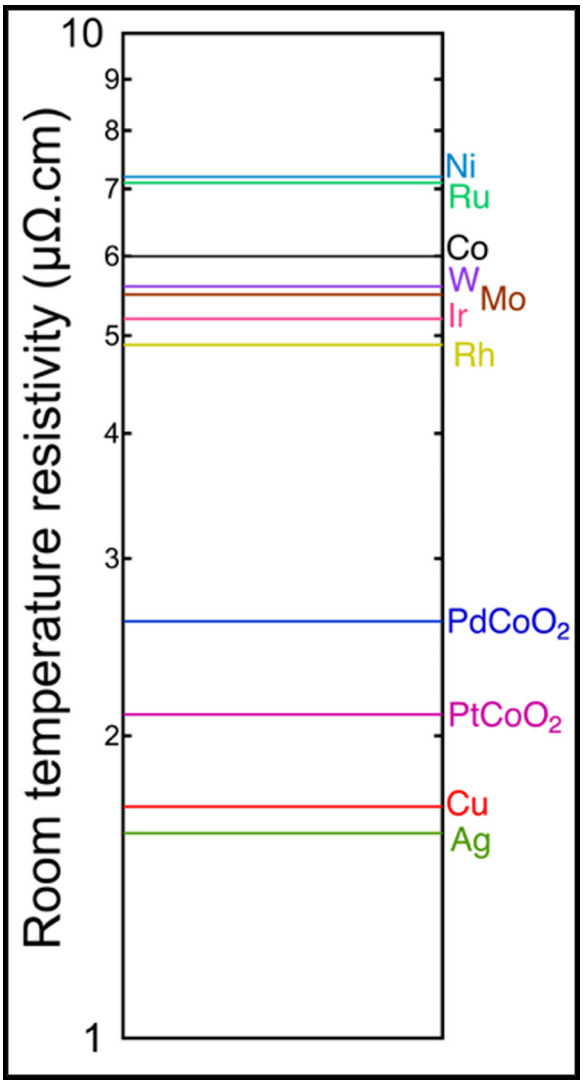

Figure 2: Comparison of room temperature resistivity of $PdCoO_2$ and $PtCoO_2$ to conventional interconnect metals.

Conclusions and Future Steps:

We have two main future goals: (1) The first goal is to characterize electrical properties in decreasing dimensions, similar to interconnect dimensions, for which we are planning to fabricate nanowires of MBE-grown $PdCoO_2$ thin films, via photolithography and e-beam lithography, and (2) the second goal is to demonstrate the growth of highly crystalline $PtCoO_2$ films via ALD and post-deposition annealing.

References:

[1] D. Gall, J. Appl. Phys. 127, 050901 (2020).

[2] V. Sunko, P.H. McGuinness, C.S. Chang, E. Zhakina, S. Khim, C.E. Dreyer, M. Konczykowski, M. König, D.A. Muller, and A.P. Mackenzie, Phys. Rev. X 10, 021018 (2020).

[3] C.W. Hicks, A.S. Gibbs, A.P. Mackenzie, H. Takatsu, Y. Maeno, and E.A. Yelland, Phys. Rev. Lett. 109, 116401 (2012).

[4] J. Sun, M.R. Barone, C.S. Chang, M.E. Holtz, H. Paik, J. Schubert, D.A. Muller, and D.G. Schlom, APL Mater. 7, 121112 (2019).

[5] Q. Song, J. Sun, C.T. Parzyck, L. Miao, Q. Xu, F.V.E. Hensling, M.R. Barone, C. Hu, J. Kim, B.D. Faeth, H. Paik, P.D.C. King, K.M. Shen, and D.G. Schlom, APL Mater. 10, 091113 (2022).

Lithography for Topological Nanowires

CNF Project Number: 3032-22
Principal Investigator(s): Jeeyoung Judy Cha
User(s): Yeryun Cheon, Khoan Duong, Han Wang, Mehrdad Kiani, Quynh Sam, Gangtae Jin

Affiliation(s): Department of Materials Science and Engineering, Cornell University

Primary Source(s) of Research Funding: The Gordon and Betty Moore Foundation's EPiQS Initiative, Grant GBMF9062; Semiconductor Research Corporations (SRC) JUMP 2.0 SUPREME; The National Science Foundation, Division of Materials Research #2240956

Contact: jc476@cornell.edu, yc2458@cornell.edu, nd399@cornell.edu, hw578@cornell.edu, mtk73@cornell.edu, qps2@cornell.edu, gj98@cornell.edu

Website(s): cha.mse.cornell.edu

Primary CNF Tools Used: Nabity System for Supra SEM, Zeiss Ultra SEM, SC4500 Odd-Hour Evaporator

Abstract:

Topological materials in nanowire forms can transform future computing technologies by enabling fault-tolerant quantum computing using topological superconductor nanowires or energy-efficient interconnects using topological semimetal nanowires. The major challenge remains synthesis of these materials in nanowires. We employ the recently developed thermomechanical nanomolding [1] to fabricate nanowires of topological materials. In this project, we fabricate nanodevices using the molded nanowires to measure their transport properties.

Summary of Research:

We have successfully molded various topological semimetals [2] and layered materials into nanowires using thermomechanical nanomolding. We have further extended the nanomolding method to two-dimensions (2D) and demonstrated wafer-scale fabrication of 2D nanostructures [3]. We are fabricated nanodevices on these molded nanostructures to test if some of the topological semimetals may be promising interconnect materials that can replace the state-of-the-art copper interconnects and to measure topological protected surfaces states in transport in these molded nanowires.

Conclusions and Future Steps:

Thermomechanical nanomolding is a promising synthesis technique that can rapidly and with scale fabricate nanowires of topological materials. We have produced several classes of topological materials into nanowires using this method. Future steps include fabrication of nanodevices using standard e-beam lithography on these molded nanowires to measure their transport properties.

References:

[1] M. T. Kiani, J. J. Cha, Nanomolding of topological nanowires, APL Mater. 10, 080904 (2022).

[2] M. T. Kiani, Q. P. Sam, G. Jin, B. Pamuk, H. J. Han, J. L. Hart, J. R. Stauff, J. J. Cha, Nanomolding of metastable Mo_4P_3, Matter doi:10.1016/j.matt.2023.03.023 (2023).

[3] M. T. Kiani, Q. P. Sam, Y. S. Jung, H. J. Han, J. J. Cha, Wafer-scale fabrication of 2D nanostructures via thermomechanical nanomolding, arXiv: 2306.10167 (2023).

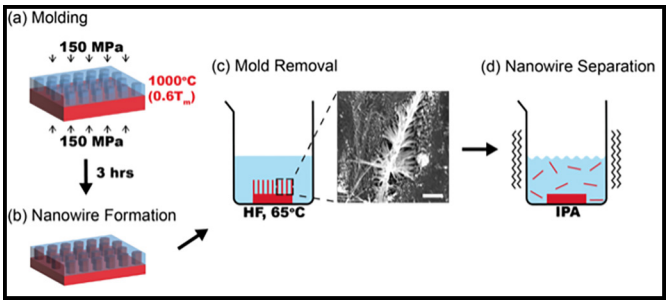

Figure 1: Schematic of thermomechanical molding. (a) Bulk feedstock of topological material (red) is pressed onto the nanostructured mold, in this case anodized aluminum oxide (blue). (b) After molding, nanowires form. (c) The molded nanowires are extracted from the mold by etching the mold. (d) the molded nanowires are separated from the bulk feedstock by sonication.

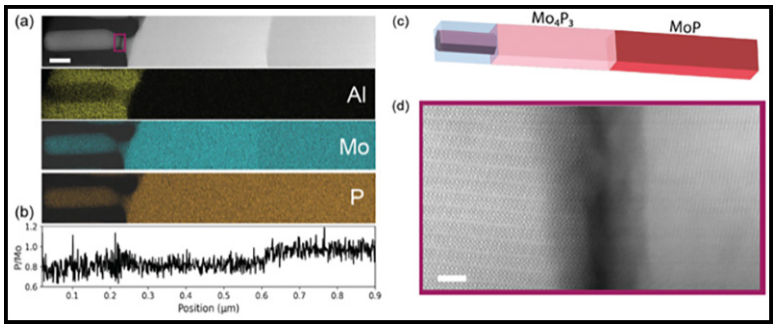

Figure 2: Thermomechanically molded Mo_4P_3 nanowires. (a) Cross-section scanning transmission electron microscopy (STEM) and chemical mapping images of the Mo_4P_3 nanowire molded into the aluminum oxide mold, with the bulk feedstock also intact. (b) The P/Mo composition changes at the mold entrance as phosphorus vapor leaves the apparatus during molding. (c) Schematic of the molding process for Mo_4P_3 nanowire. (d) Atomic-resolution high-angle annular dark field STEM image of the molded nanowire.

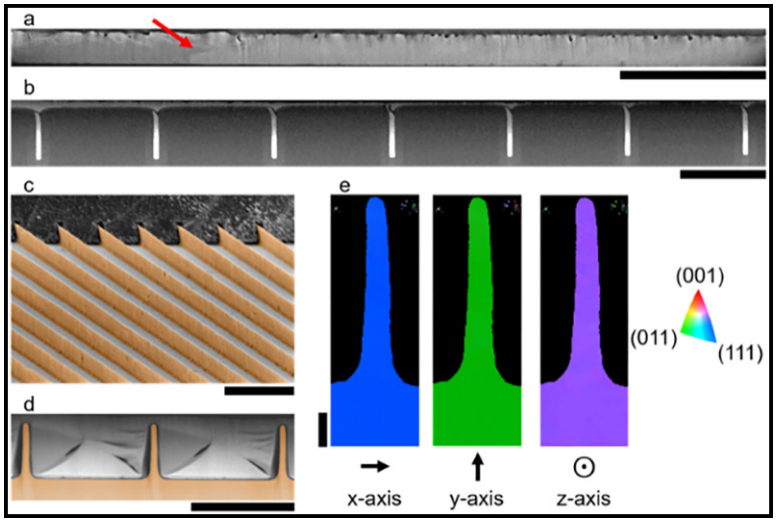

Figure 3: Nanomolded 2D Cu-filled trenches and free-standing 2D Cu fins. (a, b) Scanning electron microscopy (SEM) images of the Cu-filled trenches at the wafer scale, using Si mold. (c, d) Free-standing 2D Cu fins, after etching away the Si mold. (e) Single-crystalline Cu-filled trench at the nanoscale.

Lithography for 2D Materials

CNF Project Number: 3035-22
Principal Investigator(s): Jeeyoung Judy Cha
User(s): Shiyu Xu, Natalie Williams

Affiliation(s): Department of Materials Science and Engineering, Cornell University

Primary Source(s) of Research Funding: The National Science Foundation, CBET-CAREER #2240944

Contact: jc476@cornell.edu, sx269@cornell.edu, nlw49@cornell.edu
Website(s): cha.mse.cornell.edu

Primary CNF Tools Used: Heidelberg Mask Writer - DWL2000, SC4500 Odd-Hour & Even-Hour Evaporator

Abstract:

Intercalation is a reversible insertion of ions, atoms, and molecules into empty spaces in crystalline materials (Figure 1). For layered materials, intercalation can tune the materials properties greatly and even induce new phases. We electrochemically intercalate lithium ions into layered transition metal dichalcogenides and rare-earth tri-tellurides to induce new phases, change materials properties, and study nanoscale effects on the thermodynamics of lithium (Li) intercalation. For this, we fabricate electrochemical cells on individual nanodevices using exfoliated flakes, which allows us to measure the changes in the structure and electrical properties of the host material as we controllably intercalate lithium.

Summary of Research:

We discovered that semimetallic molybdenum ditelluride ($MoTe_2$) becomes semiconducting when enough lithium gets intercalated. The intercalation-induced semiconducting phase takes on a new crystal structure not found in existing polymorphs of $MoTe_2$, observed by Raman spectroscopy (Figure 2). We constructed electrochemical cells that are compatible with *in situ*, single-crystal X-ray diffraction experiments so that we can identify the new crystal structure. X-ray data were successfully obtained, and we are currently analyzing them. Further, we observed that the intercalation-induced phase change in these layered materials can be affected greatly by the interactions with the substrate; this is clearly observed by the intercalation-induced phase change getting delayed for thinner samples, where the substrate effects will be more enhanced. Finally, we observed that lithium intercalation into lanthanum tritelluride ($LaTe_3$) modifies the uni-directional charge density wave (CDW) that is present in $LaTe_3$. From Raman spectroscopy, it appears that uni-directional CDW gets suppressed with increasing concentrations of lithium intercalation into $LaTe_3$.

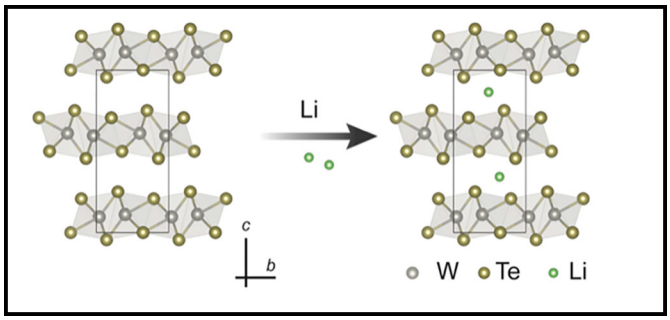

Figure 1: Schematic of lithium intercalation into tungsten ditelluride (WTe_2).

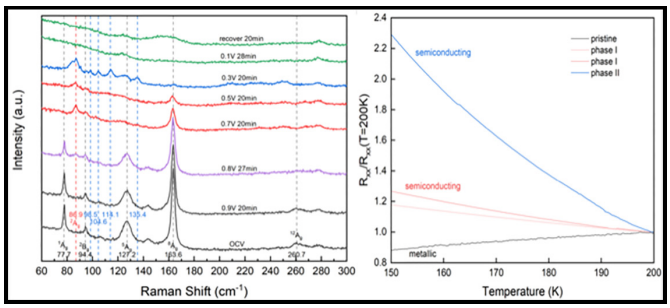

Figure 2: (Left) New structure is observed by intercalating lithium into molybdenum ditelluride ($MoTe_2$), which we denoted as Phase I and Phase II. (Right) These new phases are semiconducting, as confirmed by increasing resistance with decreasing temperature, in contrast to the initial metallic $MoTe_2$.

Conclusions and Future Steps:

Three manuscripts are in preparation to report our findings regarding lithium intercalation into layered materials: (1) new semiconducting phase in $MoTe_2$ by lithium intercalation, (2) thickness effects in intercalation-induced phase transition in WTe_2, and (3) changes in CDW in $LaTe_3$ by lithium intercalation. We will continue investigate the origin for the apparent suppression of the CDW phase in $LaTe_3$ with lithium intercalation. We will extend the study by including other rare-earth tritellurides that also have CDW phases. Transport measurements will also be carried out as a function of lithium intercalation, *in situ*.

Measuring the Mechanical and Electrical Properties of Ionically Conductive Polymers

CNF Project Number: 3058-23
Principal Investigator(s): Meredith Silberstein
User(s): Max Tepermeister, Ellen van Wijngaarden

Affiliation(s): Sibley School of Mechanical and Aerospace Engineering, Cornell University
Primary Source(s) of Research Funding: DARPA
Contact: meredith.silberstein@cornell.edu, mt845@cornell.edu
Website(s): silbersteinlab.com
Primary CNF Tools Used: DISCO Dicing Saw, Harrick Plasma Generator, Malvern Nano ZS Zetasizer

Abstract:

The mechanical and electrical properties of polymers enable their use in biosensors, biohybrid robotics and energy conversion devices. This research focused on how the mechanical and electrical properties of ionically conductive properties can be tuned for different applications. We used photolithography to fabricate an electrode setup to characterize a range of ionic polymers, revealing unexpected trends including increase in conductivity with ion size. Recent work has focused on the properties of biopolymers, specifically extracellular polymeric substances from bacteria including *Sphingomonas* and *Pseudomonas Aeruginosa*. Preliminary results demonstrate our ability to tune properties based on the blend of polymers present.

Summary of Research:

The primary goal of this research project is to characterize mechanical and electrical properties of ionically conductive polymers. This includes describing synthetic soft materials that use ionic transport as well as characterizing soft biopolymers with potential applications in ionic circuits. Traditional materials for circuit design are metal and semiconductor substrates; hard materials that are typically incompatible with biosystems. Biosystems utilize circuits to achieve environmental responses as seen in neurons and membrane ion channels. These systems have been previously studied from a biomechanical perspective, however, few reduced order circuit models have been developed. Research into soft ionic conducting materials has focused primarily on maximizing conductivity for use in electrochemical conversion and storage device membranes, with limited progress in the development of experimental wetware.

As part of this broader effort, we have experimentally characterized the ionic conductivity of a wide range of polymers. Impedance spectroscopy experiments were conducted on a Gamry 3000AE in the Silberstein lab. CNF tools were used to fabricate a gold-on-glass electrode using S1800 series photoresist patterned onto fused quartz wafers as shown in Figure 1. Electron-beam thermal evaporation was used to deposit a titanium adhesion layer followed by a gold layer. The water-jet liftoff machine was used to remove any excess gold before photopatterning spacers on the periphery of the electrodes. The SU-8 spacer can be seen in Figure 1 as the small lighter rectangles in a square around the central gold square. Impedance spectroscopy measurements were performed by adding the sample between the electrodes to create a parallel plate capacity. An oscillating electric field at various frequencies was applied to determine the electrical response of the test material. The system was used to test metal ligand coordinated polymers, polyionic hydrogels, and ionomers swollen with ionic liquids. Figure 3 depicts the ionic conductivity of a broad range of materials that have been characterized using this device.

Results showed that the ionic conductivity of ligand functionalized polydimethylsiloxane (PDMS) with metal salts incorporated was far greater than the conductivity of unfunctionalized PDMS. Additionally, the conductivity of metallo-PDMS depended on both the type of anion and cation within the salt and the salt concentration. Notably, the larger anions led to higher conductivity values despite having a lower diffusivity due to their size. This trend resulted from the larger anions dissolving into the polymer and dissociating better than smaller anions. Further details can be found in the recently published manuscript [1].

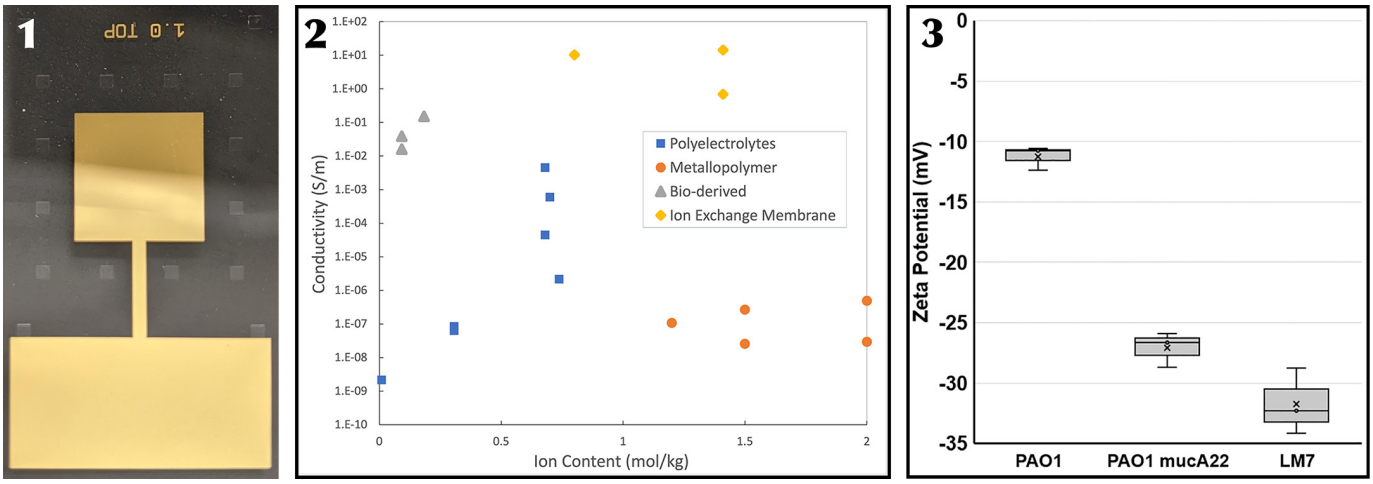

Figure 1, left: Experimental setup showing one electrode out of four on a wafer. Figure 2, middle: Conductivity vs ion content for four material classes. Figure 3, right: Zeta Potential results comparing ionic polymers from wild type Pseudomonas Aeruginosa, (PAO1), an alginate overexpression strain (PAO1 mucA22), and Sphingomonas LM7.

Initial tests completed for the characterization of biofilms have focused on a recently isolated strain of *Sphingomonas* bacteria, *LM7*. *Sphingomonas* bacteria are known for the production of high molecular weight polymers, primarily made of polysaccharides, that are widely used in applications in oil and gas as well as food processing. The work aimed to identify the initial properties for comparison to materials from other species, such as *Pseudomonas Aeruginosa*, and various material characterization methods were used to establish the properties of the *Sphingomonas* biofilms. The malvern nano-s zetasizer was used to measure molecular weight, size and zeta potential, as shown in Figure 3, to compare the biofilm from *Sphingomonas LM7* to strains of *P. Aeruginosa* and biopolymers from literature, such as gellan gum. Biofilms were grown over a period of four days before cultures were centrifuged to remove cells and the polysaccharide was removed from the supernatant using cold ethanol precipitation. Enzymes and phenol extraction were used to break down and remove DNA, RNA and proteins. The final material was dialyzed, lyophilized and then rehydrated as per zetasizer specifications for the desired measurements.

The zeta potential results from *Sphingomonas LM7* were compared to material from the well-known biofilm producer *P. Aeruginosa* wild type (PAO1) and PAO1mucA22, a strain of *P. Aeruginosa* modified to overexpress alginate, a negatively charged polymer. The zeta potential values indicate a negative charge for the *LM7* polymer similar to the PAO1mucA22 strain and significantly lower than the wild type biofilm. The value for *LM7* is similar to the values for zeta potential reported in literature for a similar biopolymer, gellan gum from another *Sphingomonas* strain [2]. Next steps will include additional materials characterization tests to better understand the ionic and mechanical properties of these biopolymers and testing a wider variety of biopolymer blends.

Conclusions and Future Steps:

The tools and technical expertise provided at the CNF was essential to the rapid design and fabrication of the experimental setup for material characterization providing novel insight into the behavior of ionic polymers. In the coming months, we will investigate device/junction through the design of additional microscale devices. We will also expand on our preliminary material tests of extracellular polymeric substances to include material from bacteria genetically modified to produce specific polymer blends.

References:

[1] Xinyue Zhang, Jinyue Dai, Max Tepermeister, Yue Deng, Jingjie Yeo, and Meredith N. Silberstein. Macromolecules 2023 56 (8), 3119-3131 DOI: 10.1021/acs.macromol.2c02519.

[2] Duarte LGR, Alencar WMP, Iacuzio R, Silva NCC, Picone CSF. Synthesis, characterization and application of antibacterial lactoferrin nanoparticles. Curr Res Food Sci. 2022 Mar 26;5:642-652. doi: 10.1016/j.crfs.2022.03.009. PMID: 35373146; PMCID: PMC8971344.